A LIDAR-BASED AUTO HYDRO BREAKLINE GENERATION ALGORITHM FOR

STANDING WATER BODIES

by

GEORGE JOHN TOSCANO

Presented to the Faculty of the Graduate School of

The University of Texas at Arlington in Partial Fulfillment

of the Requirements

for the Degree of

DOCTOR OF PHILOSOPHY

THE UNIVERSITY OF TEXAS AT ARLINGTON

August 2015

Acknowledgements

Abstract

A LIDAR-BASED AUTO HYDRO BREAKLINE GENERATION ALGORITHM FOR

STANDING WATER BODIES

George John Toscano, PhD

The University of Texas at Arlington, 2015

Supervising Professor: Venkat Devarajan

Airborne light detection and ranging (LiDAR) is a sensor that can generate terrain elevation and intensity data of very large areas with high precision and dense resolution. The intensity and elevation are co-registered, which eliminates the need for tedious registration after the fact. This combined LiDAR data can be used to classify different topographic features. Given the enormous amount of such data generated all over the world, total automation in these classification processes in a batch process is highly desired if not a critical need.

In this dissertation, a novel LiDAR-based automated standing waterbody extraction (LASWE) algorithm is presented. The special characteristics of water bodies that helped with the development of the LASWE are: a) the essentially flat surface of water bodies and b) the surface elevation of water bodies is lower than that of its surrounding areas. In addition, the special characteristics of LiDAR intensity return from the water surface, which helped with the ideation of the LASWE algorithm are: a) the specular reflection from smooth water surface and b) the spectral reflectance of water is low compared with vegetation and other topographic features.

The LASWE algorithm employs a novel histogram analysis method for segmentation of flat areas and then an SVM classifier to eliminate false detections. An

intensity-based classifier was also used to remove other false detections that were not eliminated by the SVM classifier. An iterative pixel-based maximum likelihood classification (MLC) technique was employed to fine-tune water surface detection at the land edge of water bodies. Three LiDAR datasets from different geographical locations were split into training and testing sets for validating our LASWE algorithm. The classification accuracy of the algorithm was measured by calculating the overall accuracy and the standard Cohen's kappa coefficient. The LASWE algorithm was found to give classification accuracy greater than 97.92%.

Speed of computation is of essence in all classification problems. The multiresolution LASWE (MLASWE) algorithm presented in this dissertation is an upgraded version of the LASWE, which was designed to detect water surface significantly faster than the LASWE algorithm without compromising the classification accuracy. The MLASWE algorithm detects water surface with a coarse resolution first and then with an intermediate resolution and finally, with a fine resolution in addition to using efficient buffering techniques.

In summary, the MLASWE algorithm presented in this dissertation is a robust, raster-based method that detects water surfaces at high speed, in a fully automated mode and with high accuracy.

Table of Contents

List of Illustrations

List of Tables

Chapter 1

Introduction

1.1 Background

Light detection and ranging (LiDAR) technology is widely used for mapping earth surface with high precision and accuracy. A LiDAR system can be broadly categorized as an airborne or a terrestrial system. Terrestrial LiDAR gives higher resolution and accuracy, whereas an airborne LiDAR can cover a large area in a very short time. The essential components of an airborne LiDAR system is

      a) an aircraft

      b) a laser scanning emitter and receiver unit

      c) a differential global positioning system (DGPS)

      d) an inertia measurement unit (IMU) and

      e) a computer.

Current LiDAR systems can collect samples from the earth's surface at rates greater than 150 kHz (Schmid et al., 2008).

The main advantage of airborne LiDAR over other mapping technologies is its higher accuracy, denser resolution and its ability to map the earth below the vegetation. The other advantage is that LiDAR may be the only mapping option in many geographical locations where field surveying is not possible due to low accessibility. Because of LiDAR technology, a very accurate digital elevation model (DEM), a digital terrain model (DTM), a triangulated irregular network (TIN) etc. can be obtained.

Surface water mapping is important for accurate characterization of topography for geomorphological research (French, 2003), for efficient flood management (Hollaus et al., 2005) and for surveying geomorphological change of floodplains (Jones et al., 2007).

Surface water mapping is also important to understand wetland dynamics (Jenkins and Frazier, 2010) and estimate water storage capacity in isolated wetlands (Lane and D'Amico, 2010). It is difficult to study forested wetland hydrology, since conventional remote sensing methods such as aerial photographs and multispectral images fail to see through vegetation (Lang and McCarty, 2008). LiDAR data can penetrate vegetation and can be used to detect inundation under forest canopy. Thus, LiDAR technology opens a new window for research in the field of geoscience and hydrology.

A LiDAR system records the intensity of the returned pulse from the object it maps. LiDAR intensity return represents the strength of reflection from the object at the wavelength of light used by the LiDAR system. Most of the topographic LiDAR systems use light in the near infra-red part of the spectrum, whereas bathymetric LiDAR systems use light in near infra-red and green spectrum. LiDAR elevation and intensity data are used to classify different topographic features such as water, vegetation, forests, soil saturation, roads, grass and roofs (Antonarakis et al., 2008; Brennan and Webster, 2006; Charaniya et al., 2004). Automation in these classification processes is highly desired and, is therefore a key area of interest in both commercial arena as well as in academia (Flood, M., 2001).

1.2 Motivation for current research

Classification in remote sensing can be broadly categorized as classification in urban areas and classification in rural areas. Classification in urban areas includes rooftops, roads and other man-made structures. Classification in rural areas includes water bodies, different types of forests, gravel, bare earth, wetlands etc.

In rural areas, hydro breaklines are necessary to create LiDAR derivative products such as DEM, DTM, TIN etc. Water body detection and delineation are in turn

necessary to generate hydro breaklines. Hydro-flattening follows the detection and delineation of water bodies (lakes, rivers, ponds, reservoirs, streams etc.). Manual hydro breakline generation is time consuming and expensive, especially when there are a large number of lakes, rivers and their tributaries and, a large number of vertices are marked for delineation of water bodies. Therefore, automation with minimal human intervention is desired for this operation. In this dissertation, an algorithm is proposed to automatically detect standing water bodies using both LiDAR elevation and intensity data.

1.3 Specific Problem Statement

The LiDAR-based automated standing waterbody extraction (LASWE) algorithm and the Multiresolution LASWE (MLASWE) algorithm, presented in this dissertation, were developed with an aim to hydro-flatten standing water bodies (SWB) such as ponds, lakes, reservoirs in a rural environment. The algorithms specifically exclude rivers and streams. Hydro-flattening of an SWB requires its detection and, delineation with hydro breaklines and, then the assignment of a constant elevation to it.

The training and testing dataset should be large enough in order to validate a robust LASWE algorithm applicable in different conditions.

The LASWE algorithm needs to run fast because it was developed to detect SWBs in large areas. The time required to detect water bodies per unit area should be within a limit, though no real time output is required.

The US Geological Survey (USGS) specifies that the minimum water body size to be detected should be 2 acres (Heidemann, 2012). However, our goal was to detect water bodies greater than half acre in size.

Chapter 2

Literature Review

2.1 Introduction

Classification in rural environments is an important and active research area in remote sensing. Land-use features comprise an important set within rural features. Multispectral imagery has been used by many researchers for land use classification (Duda et. al. 1999; Sun et al., 2003, Huang et al. 2002). However, in the last decade much work has been accomplished on land cover classification including water bodies using LiDAR data (Antonarakis et. al, 2008; Brennan and Webster, 2006, Charaniya et al., 2004). Gesch, D.B., (2009) and Brzank et al., (2008) used LiDAR data to detect and delineate water in coastal areas. Höfle et al., (2009) and Briese et al., (2009) used LiDAR data for water surface classification in rivers. Lang and McCarty, (2009); Lane and D'Amico, (2010) classified water surfaces in wetland areas. All these papers related to water surface classification are discussed in the following section.

2.2 Previous work

Antonarakis et al. (2008) classified river water, gravel, short vegetation and five types of forest quickly and efficiently using LiDAR elevation and intensity data without the need for multispectral imagery. LiDAR elevation data was used as a spatial and spectral segmentation tool. A vegetation height model (VHM) and an intensity model were used for the classification. The VHM was derived by calculating the difference between a terrain model and the original point cloud surface model. The overall accuracy for water pixel (5m resolution) classification was found to be 99.19%, 98.72% and 95.20% for three different areas. It is to be noted that the result was not LiDAR point classification, rather

pixel classification. There could be multiple returns from one pixel and many pixels might have returns both from land and water. If LiDAR points were classified, the overall accuracy would be lower. In conclusion, due to the dissimilarity between pixel classification and our LiDAR point based classification, a direct comparison was not possible with our results.

Brzank et al. (2008) classified water and extracted structure lines in the Wadden sea area in Netherlands. A new supervised fuzzy logic classification was used to segment water from land. The height, intensity and 2D point cloud density were the three features used for classification. They hypothesized that water points have lower elevation, lower intensity and lower 2D point density. Since intensity and 2D point density are influenced systematically by the angle of incidence, adjusted membership functions were used for those features. The weights of individual features were calculated by calculating the level of significance by the two-sided student's t-test. A threshold was calculated by finding the intersecting point between the normalized Gaussian distribution of both classes derived from the entire membership values of all points inside a training area to classify points into water and mudflat. Overall classification accuracy was recalculated by us and found to be 94.51% and 99.08% for two areas from the classification results. This enabled a comparison of our result with theirs to a limited extent on a common basis, although it must be mentioned that they didn't solve quite the same problem as ours.

Smeeckaert et al. (2013) classified water areas in both coastal and inland areas using a supervised support vector machine (SVM) classifier using features based on the height, the local point density and the local shape of 3D point neighborhood. Pixel wise misclassifications were removed by using contextual knowledge using probabilistic relaxation. However, probabilistic relaxation might have the negative impact of

exacerbating misclassification, dilating local reliability and removing very thin objects. This method resulted in classification accuracy from 88.41% to 98.85% for seven areas.

Höfle et al. (2009) classified water surfaces in a regulated river and in a pro-glacial braided river. Two important pre-processing steps were taken before segmenting and classifying water surfaces. Radiometric correction of LiDAR intensity data was performed based on the radar range equation, which accounts for spherical loss and atmospheric loss. Laser shot dropout modeling was also performed using pulse repetition frequency. Laser shot dropout occurs from water surface more than from other landscape features, due to non-Lambertian scattering behavior of water. The LiDAR point cloud was segmented by a seeded region growing algorithm using local area surface roughness, intensity density and intensity variation as parameters. A point cloud classification accuracy of 97% was obtained by them. Once again, their problem was extraction of rivers and not SWB.

Lang and McCarty (2008) classified inundated and non-inundated areas in forested wetlands using only LiDAR intensity data. Enhanced Lee filtering was used to remove noise and increase the signal to noise ratio. They found 97.6% of the inundated area was classified accurately using filtered LiDAR intensity data.

Brennan and Webster (2006) used both LiDAR elevation and intensity data to classify land cover including water surface in an object-oriented approach. Their study area consists of urban, mixed forest and wetland-estuary coastal environment. From LiDAR points DSM, DEM, intensity, multiple echo and normalized height surfaces were derived, segmented and classified using object rule based classification. The average accuracy of 10 classes was found to be 94%. It must be mentioned that in contrast to this paper, our objective was to classify a single feature, viz. SWB and accomplish that

objective using automation. Further our objective was also to use the raw point cloud with no manual preprocessing steps.

Rutzinger et al. (2012) investigated the quality of breaklines derived from DTM generated using LiDAR data. The upper and lower edges were extracted independently from the region of interest with high variability in elevation by a strategy based on curvature calculation. The detection result was compared with manually digitized breaklines.

Liu et al., (2009) used LiDAR intensity data integrated with a corresponding orthoimage for coastal zone mapping. A historical bluffline was used as a reference. 2D blufflines were made from an orthoimage and 3D blufflines ware made from the corresponding LiDAR data.

2.3 Relevance of previous work to the dissertation

In recent times, LiDAR data has been used to detect and delineate water bodies with very good accuracy. Lang and McCarty (2009) used only LiDAR intensity data to detect inundation in forested wetlands, whereas Rutzinger et al. (2012) used only LiDAR elevation data to create breaklines in glacial fluvial. Lang and McCarty (2009) showed that LiDAR intensity data gives a better classification result in forested area than digital optical imagery. Antonarakis et al. (2008) and Brennan and Webster (2006) used both LiDAR elevation and intensity data for land cover classification which also includes water surfaces. Brzank et al. (2008), Smeeckaert et al. (2013) and Höfle et al. (2009) also classified water using both LiDAR elevation and intensity data. Brzank et al. (2008) classified water in coastal areas using Fuzzy logic, where higher elevation was attributed to lower probability of the existence of a water body. In this dissertation, only in-land water bodies were detected and in-land water bodies do not necessarily have the lowest

elevation. Smeeckaert et al. (2013) classified water using a pixel based technique. However, Blaschke, (2010) pointed out that object based image analysis (OBIA) methods were showing considerable progress in information extraction in the remote sensing field.

Chapter 3

LASWE Algorithm Ideation

3.1 Introduction

The LiDAR-based automated standing waterbody extraction (LASWE) algorithm is proposed in this dissertation for detection and delineation of standing water bodies (SWB) using LiDAR elevation and intensity data. The special characteristics of water bodies which were used for the ideation of the LASWE are:

a) the surface elevation of a SWB is essentially flat

b) its elevation is lower than that of the surrounding area

c) the infra-red spectral reflectance of water is significantly lower than that of vegetation and other topographic features

d) smooth water surface causes significant specular return

The hypotheses presented in this dissertation for the LASWE algorithm are:

If an elevation histogram is plotted for a particular area containing a water body, there should be a sharp peak in the histogram because of the presence of a flat water surface. The location of the peak in the histogram represents the elevation of that water surface. The water body can be detected by detecting all the pixels that have elevations close to the peak. Some of the false detections which are caused by flat areas but not water bodies can be removed by comparing the elevation of those flat areas with their surrounding areas. The rest of the false detections can be removed by comparing the LiDAR intensity returns of those flat areas with their surrounding areas.

For the ideation of the LASWE algorithm, a knowledge of the characteristics of LiDAR intensity return is required. The characteristics of LiDAR intensity data is discussed in the following section.

9

3.2 Characteristics of LiDAR intensity returns

An airborne LiDAR system (ALS) is an active remote sensing technique which not only gives the elevation information but also the reflectance characteristics of the earth's surface in laser wavelength range. Typically, a topographic ALS system uses wavelength in near infra-red range between 800 nm to 1550 nm (Höfle and Pfeifer, 2007). Commercial LiDAR systems were able to record multiple returns (3-5) per pulse by the year 2000. Early multiple returns ALS were designed to record up to 5 returns per pulse. However, the 4th and the 5th returns occurred very rarely. Therefore, most of the LiDAR systems designed recently for topographic mapping are optimized to record 3 returns per pulse (Jensen, 2007). A LiDAR point cloud for an area in Indianapolis, Indiana is shown in figure 3-1, where the LiDAR data collection point density was 1.56 pts /m^2. Figure 3-1(a) shows the point cloud, where the points are colored based on elevation and, figure 3-1(b) shows the strength of the laser return pulses.
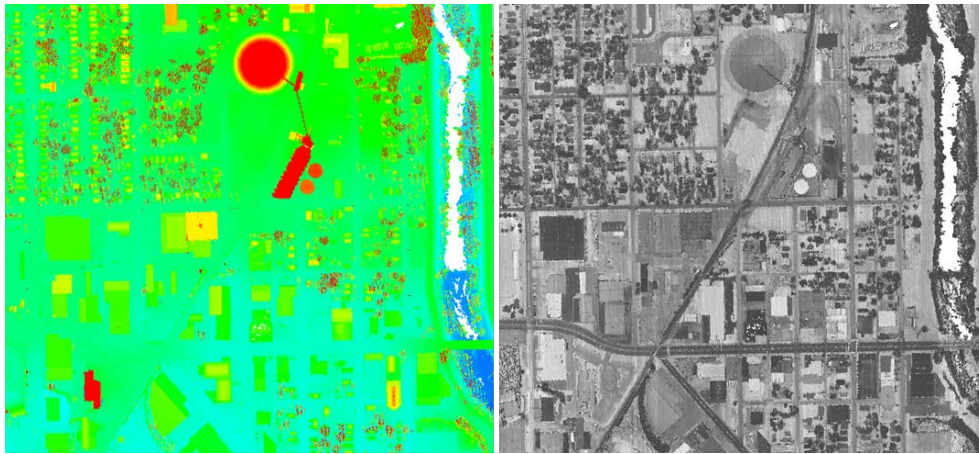
(a)   (b)

Figure 3-1 LiDAR point cloud (a) elevation and (b) intensity

A LiDAR system operates on the same principle as microwave radar but at a shorter wavelength. So the radar range equation (equation 3.1) is also valid for LiDAR (Jelalian, 1992).

$$P_r = \frac{P_t D_R^2}{4\pi R^4 \gamma^2} \eta_{sys} \eta_{atm} \sigma \qquad (3.1)$$

where: P_r is the received power

P_t is the transmitted power

D_R is the receiver aperture diameter

R is the range from sensor to target

γ is the laser beam width

η_{sys} is the system transmission factor

η_{atm} is the atmospheric transmission factor

σ is the backscatter cross section

The laser beam illuminates a circular or elliptical area when it reaches the ground or the object on the ground. This area is called laser footprint. At a typical flying height of 1000 m, the laser footprint is about 30 and 50 cm for a beam divergence of 0.3 and 0.5 mrad, respectively (Petrie et al., 2008). The dependency of the size of laser footprint to the flying height and the beam divergence is shown in figure 3-2.

The backscatter cross section in equation 3.1 is directly proportional to laser footprint and the reflectance ρ of the object. Equation 3.1 can be simplified to equation 3.2 under the following three assumptions (Jelalian, 1992):

a) The entire footprint is reflected on one surface and the target area is circular

b) The target has a solid angle of π steradians

c) The surface has Lambertian scattering characteristics
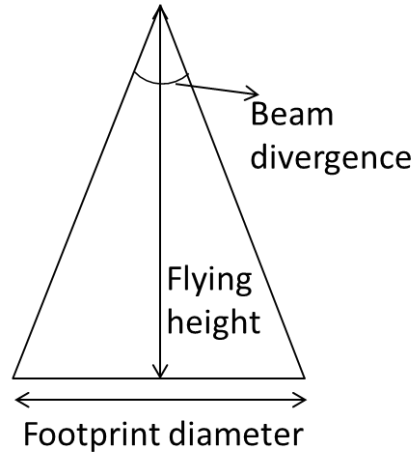
Figure 3-2 Relation of laser footprint with flying height and beam divergence

$$P_r = \frac{P_t D_R^2 \rho}{4R^2} \eta_{sys} \eta_{atm} cos\alpha_i \qquad (3.2)$$

where α_i is the incident angle.

System parameters P_t, D_R and η_{sys} can be assumed to be a constant within a flight. Therefore, equation 3.2 is further simplified to equation 3.3.

$$P_r = \frac{\rho}{4R^2} \eta_{atm} cos\alpha_i C \qquad (3.3)$$

Three variables in equation 3.3 are the reflectance ρ of the target, the range R and the incident angle α_i. Most of the topographic LiDAR systems operate in near infra-red spectrum. In the infra-red spectrum, the absorption of radiation by water bodies is higher than that of soil and vegetation (Wolfe and Zissis, 1989). So the LiDAR intensity return from the water surface is significantly lower than that of the land surface. The penetration depth of infra-red laser is also very low in water because of its strong attenuation coefficient (Campbell, 2002).

12

There are two types of reflections. They are specular or mirror-like reflection and diffuse reflection as shown in figure 3-3. Specular reflection occurs from glass, water or
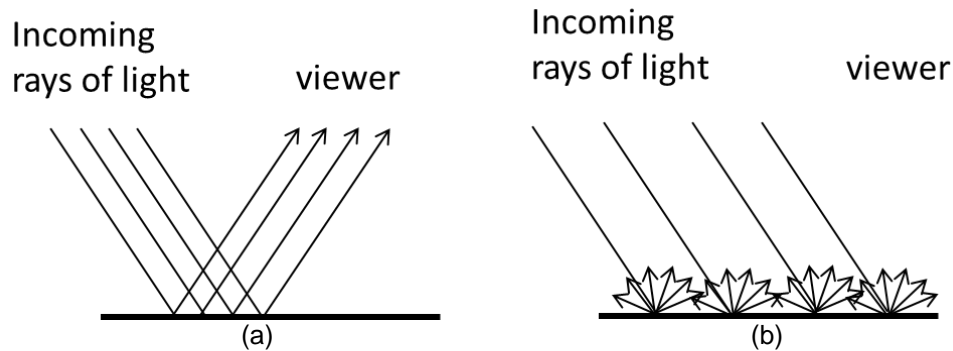
Figure 3-3 Basic reflection types (a) specular reflection and (b) diffuse reflection

smooth wet surface, whereas diffuse reflection (Lambertian reflection) occurs from rough surfaces. Most of the natural surfaces are rough. Light from all points on the surface reaches the viewer in case of diffuse reflection. Reflection off rough surfaces such as clothing, paper, wood etc. leads to diffuse reflection, whereas reflection off smooth surfaces such as a mirror or a calm body of water leads to specular reflection. If specular reflection occurs in the nadir regions of a flight line, where the angle of deflection α_d is close to zero and, if the surface of object is horizontal (angle of incidence $\alpha_i = \alpha_d$ for horizontal surface), relatively very high value signal power will reach the receiver (Höfle et al., 2009). In figure 3-4, the specular reflection from two different types of surfaces is shown.

The received signal power decreases very rapidly with the increase of deflection angle in case of specular reflection compared with diffusion reflection (Brzank et al., 2008). This phenomenon is observed, when frequent laser shot dropout occurs from the water surface at a high deflection angle.
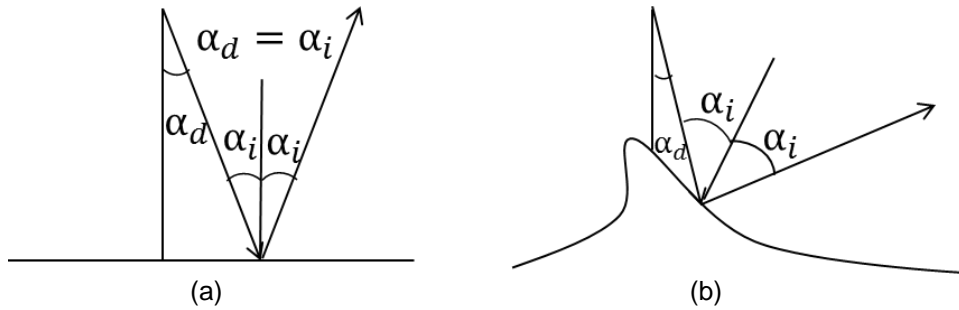
Figure 3-4 Specular reflection on (a) horizontal and (b) tilted surfaces

Brzank et al. (2008), Smeeckaert et al. (2013) and Höfle et al. (2009) used LiDAR shot dropout as one of the parameters for detecting water bodies. However, our investigation found that if the deflection angle is small, LiDAR shot dropout rates from land and water are not distinguishable. This hypothesis was studied by analyzing LiDAR data density in an area containing some water bodies. In figure 3-5, LiDAR data density per square meter is shown as pixel intensity and it can be observed that in the overlapping area of LiDAR swaths, the density of LiDAR data is high. Fourteen 10m by 10m areas were chosen for studying LiDAR shot dropout. Seven of those small areas are in the region where the deflection angle is small, and seven of those areas are in the region where the deflection angle is large. Six of those areas are from water surfaces and eight of those are from land. The density count result for low deflection angle is shown in table 3-1 and for high deflection angle is shown table 3-2. It can be seen that there is a significant difference in point density from land and water when the deflection angle is high. However, when the deflection angle is low there is no distinguishable difference.
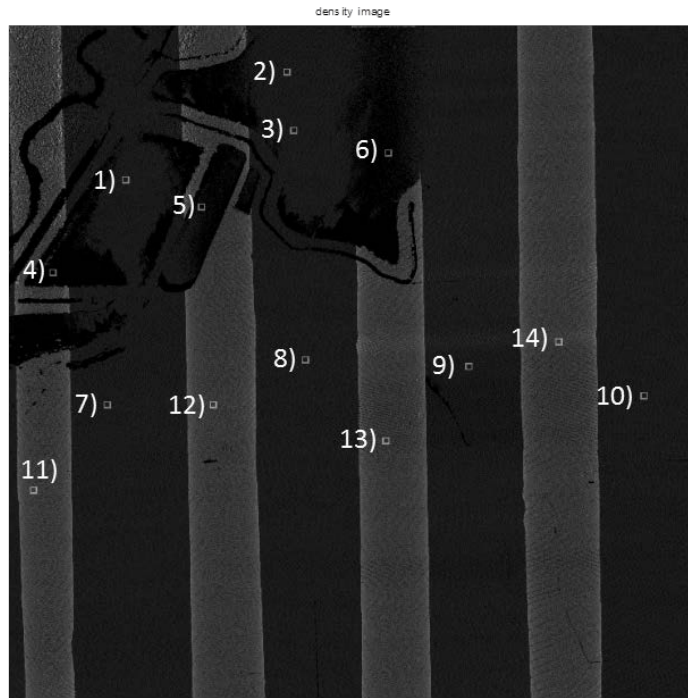
Figure 3-5 LiDAR return density for an area in L'Anguille river basin

Table 3-1 LiDAR data point density when deflection angle is low

Water		Land	
Area number	Point density Per sq. meter	Area number	Point density Per sq. meter
1	2.61	7	2.63
2	2.51	8	2.59
3	2.50	9	2.52
		10	2.53

Table 3-2 LiDAR data point density when deflection angle is high

Water		Land	
Area number	Point density Per sq. meter	Area number	Point density Per sq. meter
4	0	11	5.70
5	1.08	12	5.54
6	0.3	13	4.88
		14	5.50

3.3 Image Segmentation Techniques

LiDAR irregular point cloud data can be rasterized to get 2D elevation and intensity image. Therefore, waterbody detection using LiDAR elevation and intensity data can be treated as an image segmentation problem. Many standard image segmentation techniques such as thresholding, clustering methods, compression-based method, histogram-based method, edge detection, region-growing method, partial differential equation-based method etc. can be found in the literature. Some of these methods and their applicability in this dissertation are discussed in the following paragraph.

Sahoo et al. (1988) presented a survey of different thresholding techniques. Thresholding techniques can be classified as global and local techniques. Global thresholding can be classified as point dependent and region dependent techniques. The Otsu method (Otsu, 1975), a point dependent global thresholding technique, is based on a discriminant analysis. Relaxation method, a region dependent global thresholding technique, was introduced by Southwell et al. (1940). Thresholding is a very popular technique. It worked effectively for us as a part of the LASWE algorithm.

Haralick and Shapiro (1985) described three types of region growing techniques for segmentation. These are single linkage region growing, hybrid linkage region growing

and centroid linkage region growing techniques. Single linkage region growing technique is simple and therefore, attractive. Höfle et al. (2009) used this technique to distinguish water surface from land. The main challenges of region growing algorithm are finding a proper seed to grow and determining proper growing criteria.

3.4 Classification Techniques in Remote Sensing

The most popular classification techniques used in remote sensing are neural network classifier (NNC), maximum likelihood classifier (MLC), decision tree classifier and SVM. Smeeckaert et al. (2013) classified water employing a supervised SVM classifier using features based on the height, local point density and local shape of the 3D point neighborhood. Bartels and Wei (2006) used LiDAR based MLC fused with co-registered spectral bands for land cover classification. Brzank et al. (2008) used supervised fuzzy classification for detecting water surface.

Huang et al. (2002) compared the performance of an SVM classifier for land cover classification with an MLC, a Neural network classifier (NNC) and a decision tree classifier. SVM was found to give better classification result compared with the ML classifier and the decision tree classifier. The performance of SVM depends on the choice of the kernel parameter. The performance of NNC is also influenced by the choice of the network structure. SVM was found to perform better than NNC for some training cases and vice versa.

Wang et al. (2004) compared the MLC at the pixel level, nearest neighbor classification at the object level and, a hybrid classification that integrates the pixel-based MLC and object-based nearest neighbor method for mapping mangrove. Their studies found the hybrid classification to perform better.

Therefore, for the LASWE algorithm the SVM method or the NNC could be potential candidates for object-based classification and, pixel-based MLC could be used to fine tune the detection of SWB.

3.5 Overview of the LASWE Algorithm

Based on previous work and the ideation process described in the previous section, a novel approach was taken to detect and delineate standing water bodies with very little pre-processing of data. The algorithm was named as LiDAR-based automated standing waterbody extraction algorithm or LASWE algorithm in short. The LASWE algorithm employs the integration of object-based and pixel-based classifications. The object based classification includes a novel threshold-based histogram analysis method for segmentation using only the elevation of LiDAR returns. False detections were removed by an SVM classifier after segmentation. However, the SVM classifier was not able to eliminate all the false detections. An intensity-based classifier was designed to remove those false detections. The output was then fine-tuned by a pixel-based classification technique called maximum likelihood classification (MLC) using LiDAR intensity data.

Since the surface of a water body is almost flat, if a histogram is created based on the elevation, a peak is generally noticed at the corresponding elevation in the histogram (Toscano et al., 2013). Peaks were also found in the elevation histogram for flat surfaces which were not water bodies. Therefore, all the flat areas were detected by finding the peak locations in the histogram followed by connected component analysis. Thereafter, an SVM classifier was trained to eliminate the flat areas which were not water bodies. All the water bodies greater than half acre in size were detected. The continuity

and the size of the flat areas and the elevation profiles of the terrains surrounding the flat areas were used as input features to the SVM model.

The separation accuracy between land and water was improved by using LiDAR intensity data and elevation data as inputs to a MLC. Thereafter, the LASWE algorithm was validated by comparing its classification accuracy with that of a manual detection approach.

Chapter 4

Detailed Description of the LASWE Algorithm

4.1 Introduction

In this chapter, the LASWE algorithm is described step by step. The LASWE algorithm started with creating an elevation and an intensity raster using LiDAR point cloud data. Then water bodies were detected by a novel threshold-based histogram analysis method. False detections were removed by an SVM classifier and intensity-based classifier. Boundary of detected water bodies were fine-tuned by relaxation-based maximum likelihood classifier (MLC). Then hydro breaklines were generated. The flowchart of the algorithm is shown in figure 4-1. The details of the flowchart will be discussed after introducing the study area where the algorithm was tested.

4.2 Study Area

Three study areas were chosen for training and testing the proposed LASWE algorithm for water body detection. The description of the study areas are given in table 4-1.

Table 4-1 Study Area

Dataset	Area (in km^2)	Area Characteristics	Point density (per m^2)	Location	
				Top right	Bottom left
1. Nebraska	28.18	Mostly flat	0.4	$103^o35'37.6"$W $41^o58'46.5$N	$103^o28'8.8"$W $41^o54'38.3"$N
2. Oklahoma	178.9	Flat with some hilly terrain	0.7	$98^o0'0.1"$W $35^o48'46"$N	$97^o33'45.3"$W $35^o14'59.1"$N
3. Arkansas	11.25	Flat agricul-tural land	2.8	$90^o48'12.2"$W $35^o35'16.4"$N	$90^o44'47.3"$W $34^o47'24"$N
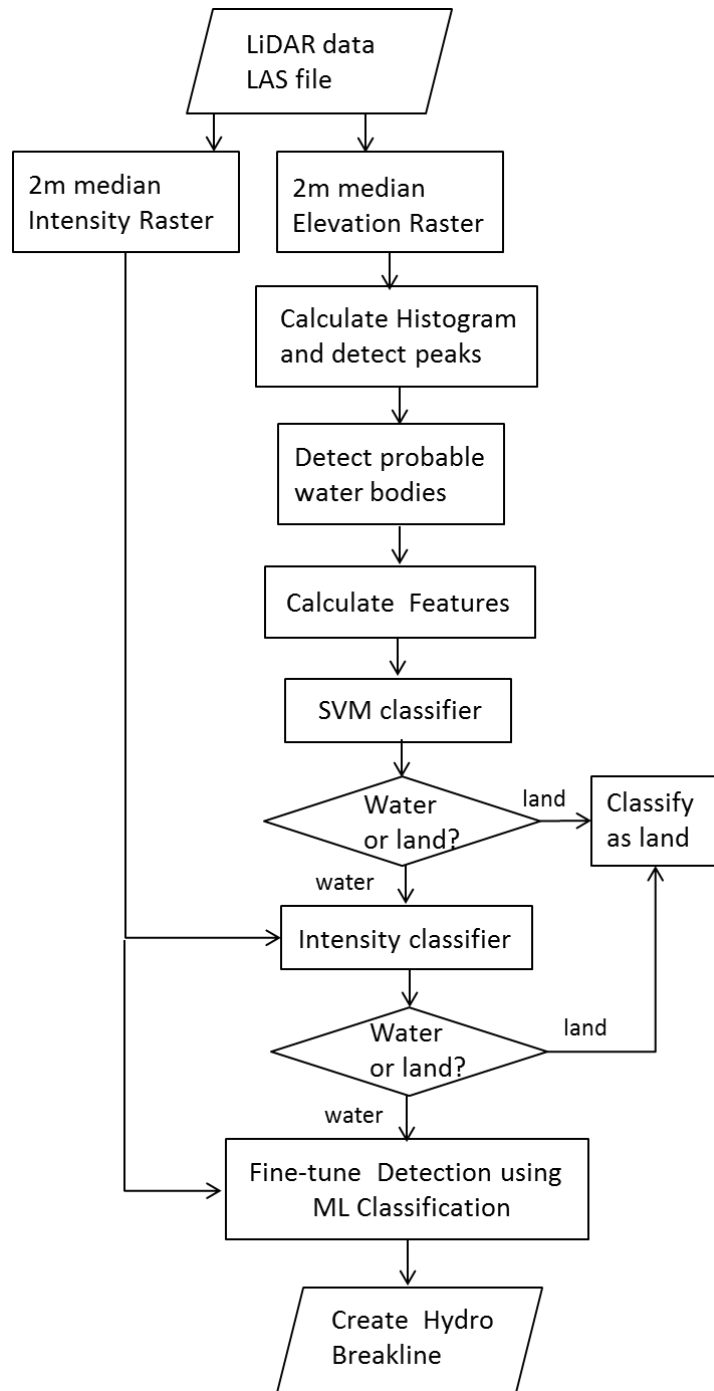
Figure 4-1 Flow chart of the LASWE algorithm

The first dataset is in Nebraska situated to the north east of Scottsbluff city. The second dataset is close to the Oklahoma City. The third dataset is in Arkansas in L'Anguille river basin. The testing and training areas for the second dataset are shown in figure 4-2.
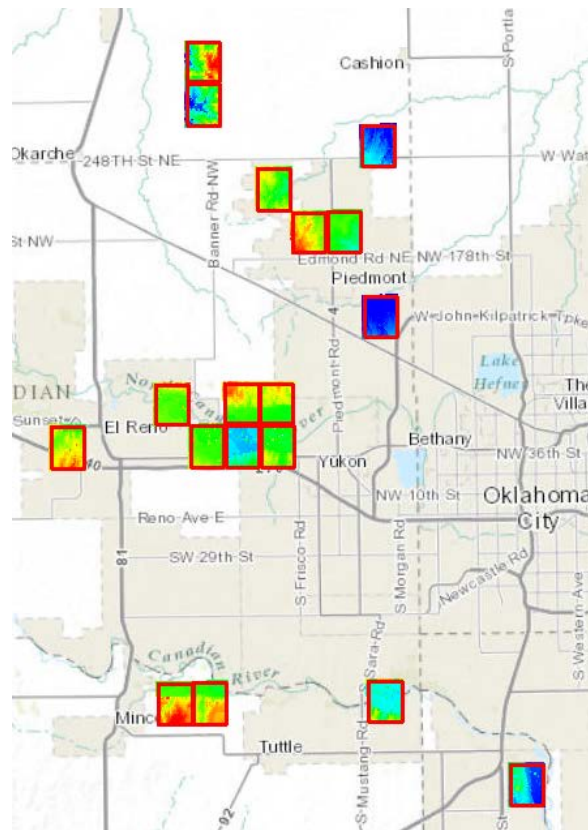
Figure 4-2 Oklahoma train and test area

4.3 Rasterization of elevation and intensity data

The elevation and intensity data were rasterized, since the point cloud is not a regular, equally spaced grid. Point cloud based approach can admittedly give us more accurate result, but processing of such data is complex and time consuming. If higher

level of accuracy is needed, point cloud data can be used around the hydro breaklines generated using the comparatively simpler raster based method.

The cell size was chosen such that the number of LiDAR returns that fall in a cell varies from 1 to 16. Therefore, a 2m x 2m cell size was considered for the LiDAR dataset. At first, the area was divided into a 2m x 2m square grid. All the single returns and all the last returns (in case of multiple returns) were retained within each 2m x 2m square. Thereafter, the median elevation value of those LiDAR returns were calculated and assigned as the elevation of each 2m x 2m square. Interpolation methods such as the inverse distance weighted method, kriging etc., are generally used for DEM generation. However, for the LASWE algorithm, the median elevation value was selected to avoid some high elevation last returns, which might not be from the ground. Median value effectively removes white noise and salt–and-pepper radar spackles, while preserving sharp shoreline edges (Liu et al. 2011). Zero elevation and zero intensity values were given to squares from which no LiDAR return was recorded.

To create the 2m pixel intensity image, each 2m x 2m square was represented by the median of all the intensity values of the single returns and, last returns (in case of multiple returns) of the point cloud that fall in that square. Median intensity value can provide a better approximation of the intensity, since it is not affected by the few excessively high and low values in the square. The 2m elevation raster and the 2m pixel intensity image for a particular test area in Oklahoma is shown in figure 4-3. Each pixel represents a 2m x 2m square in the figure.

(a) 2m elevation raster   (b) 2m pixel intensity image
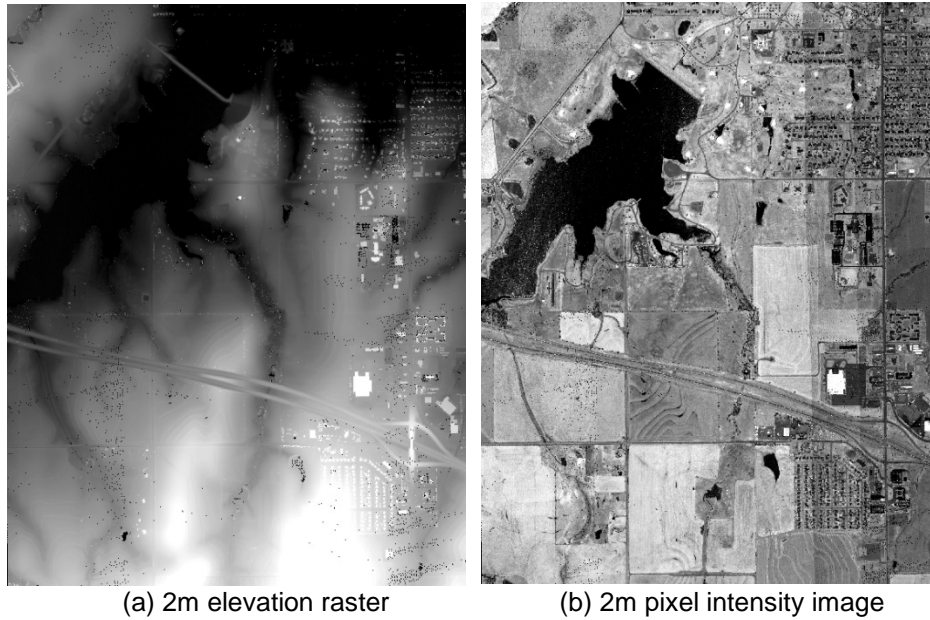
Figure 4-3 2m elevation raster and pixel intensity image for a test area in Oklahoma

4.4 Detection of sharp peaks from elevation histogram

The elevation histogram was created from the elevation raster to detect the flat areas. It was found that on the one hand, a smaller bin size for the histogram unnecessarily increases the complexity of the overall algorithm and, on the other hand a larger bin size lacks precision in water body detection. The bin size for the elevation raster was chosen to be one inch as a reasonable compromise. This bin size is independent of any other parameters.

The whole test area was divided into 500m by 500m small overlapping tiles. The overlap between adjacent tiles was chosen to be 20 percent. This small tile size was chosen to accelerate the detection process and to detect small size water bodies, which might not appear as a peak if large tile size was used. Two such tiles are shown in figure 4-4. The elevation histograms for those tiles are shown in figure 4-5. Each bin represents an elevation and the frequency of a bin represents the number of pixels with the same

elevation in the histogram. The elevations shown in the histogram of figure 4-5 are above a reference minimum elevation (in this case 403.6 meters).
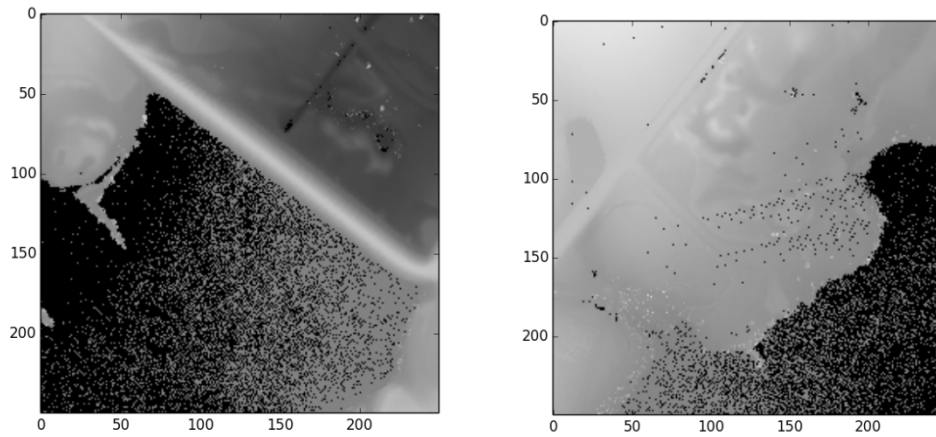
(a) Tile 1   (b) Tile 2

Figure 4-4 Elevation raster for two particular tiles

4.4.1 Modification of the histogram to compensate for LiDAR shot dropout

Sometimes a high LiDAR shot dropout rate is observed from the water surface, especially when the deflection angle is large. In those cases, due to the lack of data, a peak might not be observed at the water surface elevation location in the elevation histogram. Modifying the elevation histogram by artificially creating some elevation pixels solved this problem. The artificial elevation pixels were given elevation values according to the elevation of the scattered pixels from which LiDAR return was recorded inside the void or the connected area from which no LiDAR return was recorded. This was how the missing pixels of the elevation raster were generated for the histogram. This is a reasonable step because of the no LiDAR return pixels, the peak might not appear in the histogram or the peak position might be changed by fractional inches to a few inches.
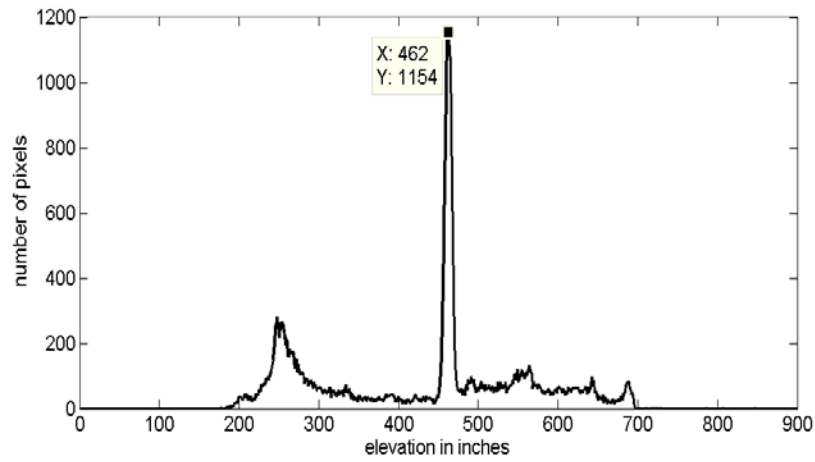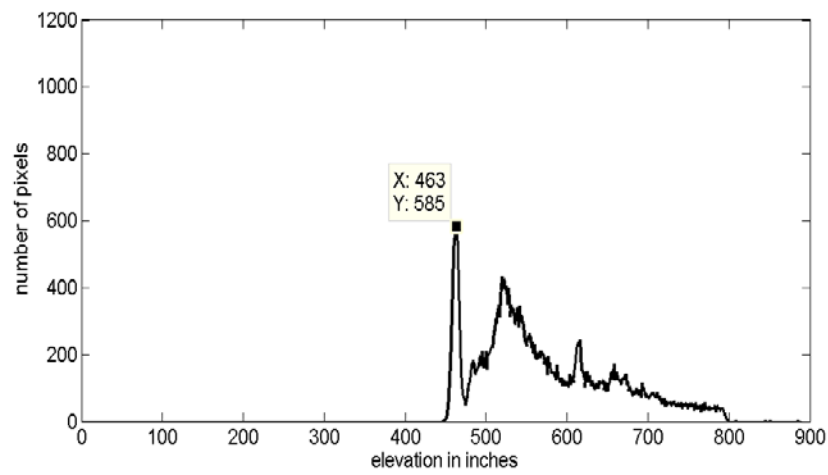
Figure 4-5 Elevation histograms for (a) tile 1 and (b) tile 2 of figure 4-4

Let the total number of voids (connected pixels from which no LiDAR return was recorded) inside a tile be *N* and, the actual elevation histogram for the tile be $h_a(x)$. A modified elevation histogram $h_m(x)$ for the tile can be expressed as equation 4.1

$$h_m(x) = h_a(x) + \sum_{i=1}^{N}\left(v_i/n_i\right)h_{ni}(x) \tag{4.1}$$

Where v_i is the data void size for the ith void, n_i is the number of scattered pixels and $h_{ni}(x)$ is the distribution of those pixels inside the ith void. It should be noted that pixels in large clusters might represent an island inside the water body and for this reason, the statistics of only the scattered pixels were taken into account for the modified histogram calculation. Modified elevation histograms are shown in figure 4-6 for the tiles shown in figure 4-4.

4.4.2 Enhancing the elevation histogram by Gaussian histogram correlator

After modifying the elevation histogram, it was correlated with a Gaussian kernel to remove spurious peaks and to precisely determine the water surface elevation (Toscano et al., 2014). The impulse response of the one-dimensional Gaussian correlator used is given in equation 4.2.

$$g(x) = \frac{1}{\sqrt{2\pi}.\sigma} e^{-\frac{x^2}{2\sigma^2}} \tag{4.2}$$

The parameter of this correlator was determined by statistical analysis of LiDAR returns from water bodies (Toscano et al., 2015). The standard deviation of the Gaussian correlator was calculated from three selected 200m*200m areas (area (a), area (b) and area (c)) from three different water bodies shown in figure 4-7. The standard deviations of the elevation in these areas were found to be 1.9233, 1.6721 and 1.3482 inches respectively. The root mean square value of the standard deviations of elevation is

$$\sigma_{rms} = \sqrt{\left(\frac{\sigma_1^2 + \sigma_2^2 + \sigma_3^2}{3}\right)}$$

$$= 1.6646 \text{ inches}$$
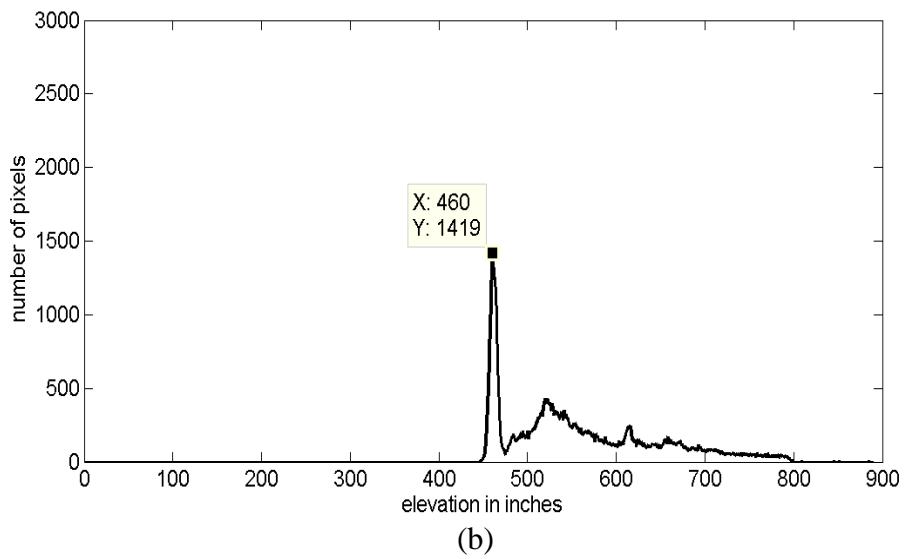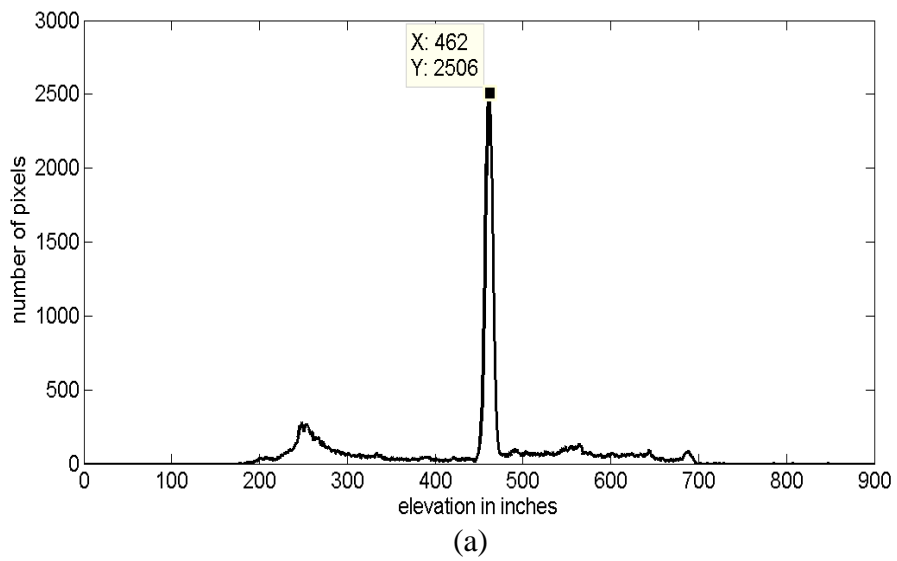
Figure 4-6 Modified elevation histograms for (a) tile 1 and (b) tile 2 of figure 4-4

(a)   (b)   (c)
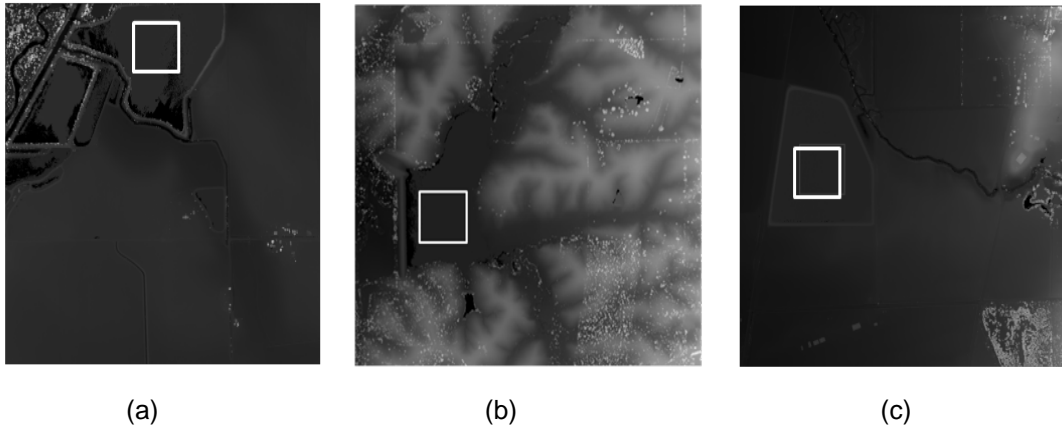
Figure 4-7 Three 200m*200m areas selected for water surface elevation standard

deviation calculation

The kernel length required for the FIR Gaussian correlator is $\lceil 6\sigma_{rms} - 1 \rceil$ or 9. The coefficients for the Gaussian correlator were determined to be [0.0134, 0.0472, 0.1164, 0.2001, 0.2397, 0.2001, 0.1164, 0.0472, 0.0134] using equation 4.2. The coefficients are shown in figure 4-8. After correlating, smoothed/enhanced histograms are shown in figure 4-9(a) and 4-9(b).
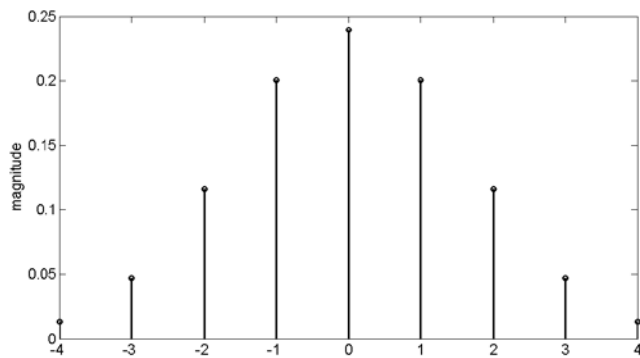
Figure 4-8 Gaussian histogram correlator used for enhancing the histogram
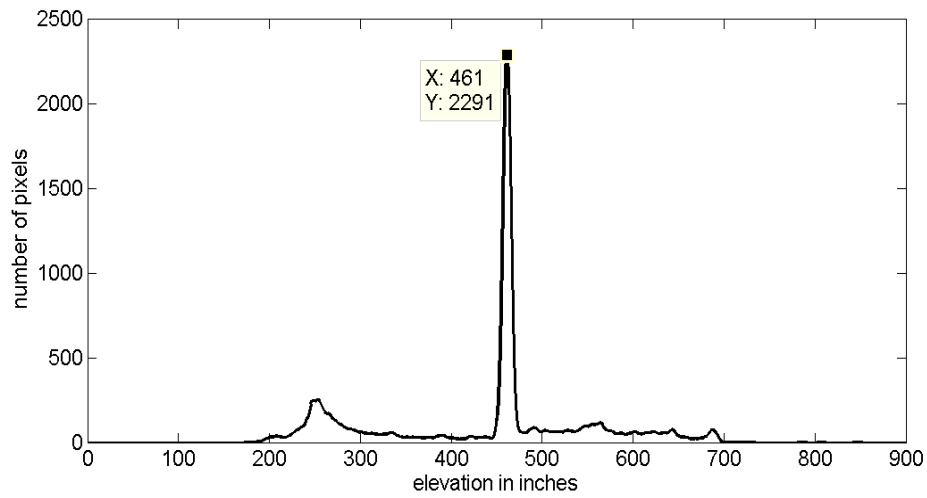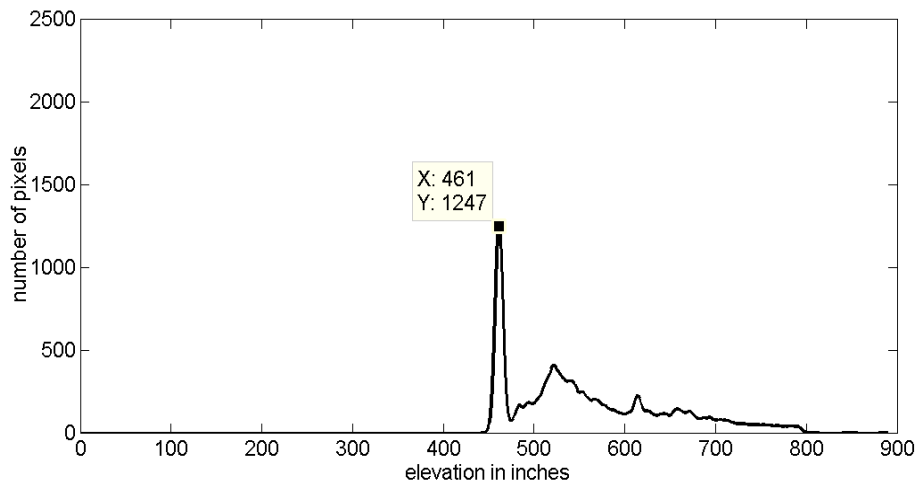
Figure 4-9 Smoothed elevation histograms for a) tile 1 and (b) tile 2 of figure 4-4

4.4.3 Determination of sharp peak locations in the histogram

The peak locations in the smoothed histogram were determined using a cubic spline data interpolation technique. Data points at adjacent bin locations in the histogram were connected by cubic spline interpolation. Each spline (between two adjacent bins with elevation x_i and x_{i+1}) can be represented by equation 4.3.

$$f_i(x) = a_i x^3 + b_i x^2 + c_i x + d_i \qquad (4.3)$$

The total number of spline equations obtained was less than the total number of bins by 1. By calculating the first derivative, the splines associated with the maxima and the minima can be determined. The first derivative of $f_i(x)$ is given in equation 4.4.

$$f'_i(x) = 3a_i x^2 + b_i x^2 + c_i \qquad (4.4)$$

$$f'_i(x) = 0 \qquad (4.5)$$

Let the solution of equation 4.5 be x_a and x_b. If x_a or x_b is real and has a value between x_i and x_{i+1} then it can be assumed that a maximum or a minimum exists in the spline between x_i and x_{i+1}. To determine whether it is a maximum or a minimum, the second derivative of $f(x)$ is calculated. For the histogram in figure 4-9(a), the total number of maxima was found to be 525. The maxima or peaks due to the presence of water bodies generally have large curvature (absolute value) at the peak. The equation to calculate curvature is given in equation 4.6

$$\kappa = \frac{|f''|}{(1+f'^2)^{3/2}} \qquad (4.6)$$

Since at the maxima $f'(x) = 0$, the equation for calculating curvature reduces to

$$\kappa = |f''| \qquad (4.7)$$

From experiment, it was found that all the peaks that have curvature less than -5 can be analysed for water body detection. For the histogram in figure 4-9(a), such peaks were found at elevation 248.28, 253.43 and 461.42 inches above the reference elevation

31

of 403.598 meters. The curvatures of those peaks, considered as sharp peaks, were [-7.1096, -5.4256, -113.46]. It was found that the portion of the water body in figure 4-4(a) corresponds to the peak at elevation 461.42 inches. The other peaks correspond to a normal flat area. The zoomed version of the sharp peak at elevation 461.42 inches is shown in figure 4-10(a).

For the area shown in figure 4-4(b), sharp peaks were found at elevation [461.33, 483.84, 521.64, 614.42] inches above reference elevation with curvature [-64.75, -6.55, -5.72, -9.05]. The peak at 461.33 inches elevation (this peak is very close to the peak at 461.42 inches, since they are part of the same water body) corresponds to the large water body. The zoomed version of the sharp peak at elevation 461.33 inches is shown in figure 4-10(b).

4.5 Detection of probable water bodies around sharp peaks

Since water surface is flat, it is highly probable to find surface of water bodies in a certain range of elevation around each sharp peak. For each of the sharp peaks, all the pixels were detected which fall in the elevation range (peak elevation – lower limit) to (peak elevation + upper limit). The upper limit and the lower limit values should be chosen in such a way so that they maximize the probability of including all the pixels from water bodies and minimize the probability of including any pixel from land. The standard deviation of elevation (σ_{rms}) calculated from water surface was found to be 1.6646 inches in section 4.4.2. Table 4-2 shows the percentage of pixels that will be excluded form detection for different choice of upper limits and lower limits for three different water surfaces shown in figure 4-7.

32

(a)

(b)
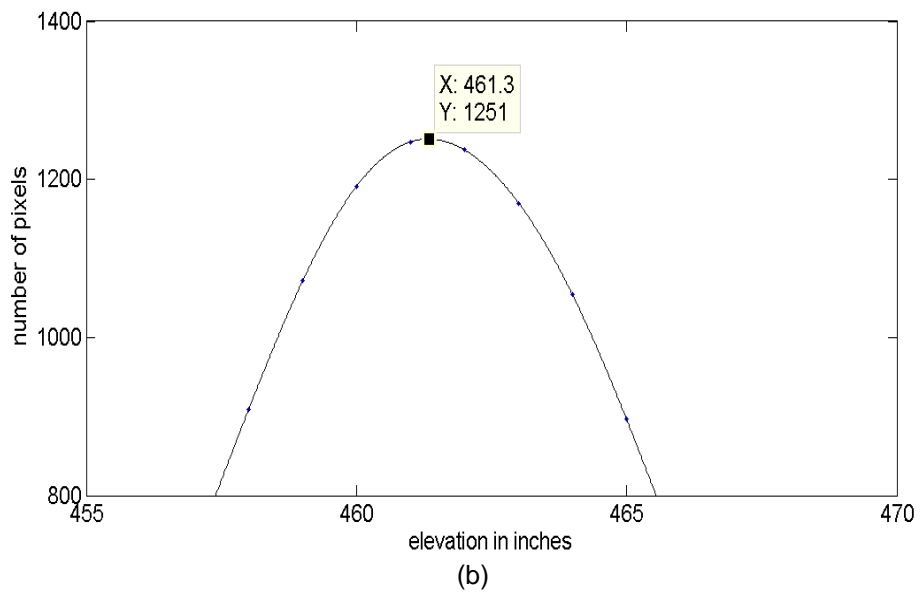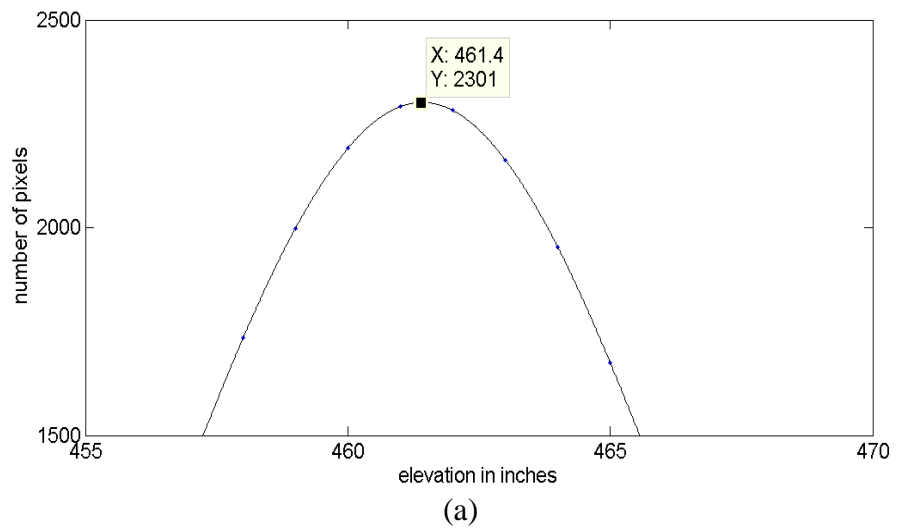
Figure 4-10 Smoothed elevation histograms (zoomed to a single peak) in figure 4-9 after

cubic spline interpolation

Table 4-2 Percentage of water pixels excluded vs upper limit and lower limit ranges

Upper limit/ lower limit (in inches)	Upper limit/ lower limit (in terms of σ_{rms})	Percentage of water surface pixels excluded from detection for different choice of upper and lower limits					
		Area (a)		Area (b)		Area (c)	
		upper	lower	upper	lower	upper	lower
1	0.6	17.08	46.61	14.79	44.34	7.45	55.06
2	1.2	9.79	14.31	7.14	16.33	2.26	19.97
3	1.8	5.55	1.66	3.36	1.62	0.34	2.45
4	2.4	3.46	0.80	1.77	0.12	0.08	0.19
5	3	1.77	0.36	0.71	0.03	0.02	0.03
6	3.6	1.09	0.19	0.40	0.02	0	0
7	4.2	0.58	0.12	0.19	0	0	0

It can be seen from table 4-2 that if the *lower* limit is chosen to be 7 inches or 4.2σ_{rms} then 0.12%, 0% and 0% of the water pixels that have elevation lower than the peak elevation will not be detected for area (a), (b) and (c) respectively. For this case, there are no misclassifications (since water surface has lower elevation than that of its surrounding area). However, if 7 inches or 4.2σ_{rms} is chosen as *upper* limit then a large number of land pixels from the land/water boundary will be included in the detection. Therefore, an optimum value of 4 inches or 2.4σ_{rms} was chosen as the upper limit. However, this choice of upper limit failed to detect some water pixels that have elevation higher than the peak elevation (from histogram) by 4 inches or 2.4σ_{rms}. For areas (a), (b) and (c), the choice of the upper limit causes an exclusion of 3.46%, 1.77% and 0.08% of water pixels respectively, as seen from table 4-2. However, most of these excluded water pixels fall inside the water body, which can be included or redetected by morphological closing operation, unlike the ones on the land/water boundary.

Some pixels from the land could potentially also be detected as water pixel, if at the land/water boundary the elevation difference between water surface and land surface

is very small. This type of error could be removed using relaxation-based ML classification discussed later.

For the sharp peak at elevation 461.42 inches, all the pixels were detected which were in the range from (461.42-4.2σ_{rms}) or 454.42 inches to (461.42+2.4σ_{rms}) or 465.42 inches for the tile shown in figure 4-4(a). The detected pixels are shown in figure 4-11. Then all the pixels from which no LiDAR return were recorded (shown in figure 4-12), were added (logical OR operation) with those detected pixels. Thereafter, using a connected component analysis, only the areas greater than half acre in size were kept. The resultant binary raster for the peak at elevation of 461.42 inches is shown in figure 4-13.
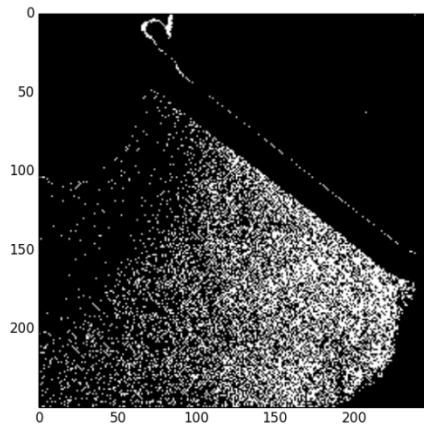
Figure 4-11 Pixels within elevation range from 454.42 inches to 465.42 inches for the tile in figure 4-4(a)
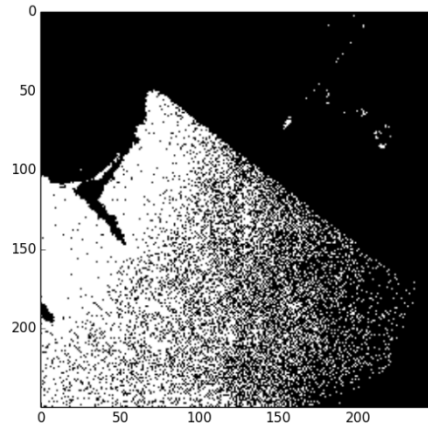
Figure 4-12 Pixels from which no LiDAR return were found for the tile in figure 4-4(a)
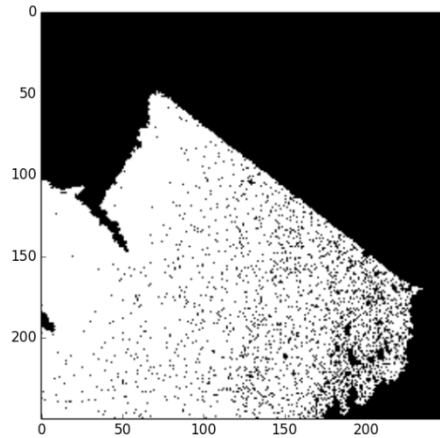
Figure 4-13 Binary raster created by adding all the pixels in figure 4-11 and 4-12

For each of the sharp peaks, flat areas greater than half acre in size were detected using the same method. The primary detected flat areas were identified as probable water bodies in this dissertation, since there could be many false detections with the actual water bodies. For the tile shown in figure 4-4(a), all the false detections (top right corner) together with the correct detection are shown in figure 4-14. In the following section, the SVM model to remove the false detections is described.
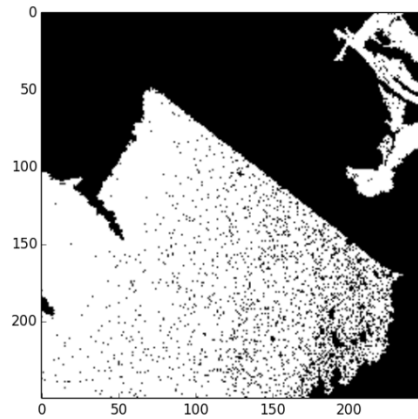
Figure 4-14 False and correct detections for the tile shown in figure 4-4(a)

4.6 SVM model training and removing false detections

In an earlier reported work (Toscano et al., 2014), four stages of filtering were used to remove the false detections using many hard coded thresholds. In this dissertation, a new SVM model was trained to identify the false detections without using hard coded thresholds. The SVM model gives a more robust result, applicable in different geographic locations compared to the previously developed threshold-dependent filtering method. To train the SVM model, an area containing plenty of water bodies from the Arkansas dataset, Oklahoma dataset and Nebraska dataset were chosen. Some randomly chosen areas from the same dataset were used for testing purposes. The input features used for the SVM model were:

i)   The continuity of the detected area

ii)   The size of the detected area

iii)   The elevation profile of the surrounding area and

iv)   The median elevation difference between the detected area and the surrounding area.

A brief description of each of the input features is given in the following section:

4.6.1 Continuity of the detected area

Water bodies must be continuous and should not contain too many non-water pixels. Non-water pixels inside a probable water body appear as gaps in the binary raster (figure 4-13). Closing the gaps inside a water body increases the number of its pixels. A dilation operation followed by an erosion operation was performed with a 7 * 7 structuring function (shown in figure 4-15) to close the gaps. All the gaps, which had smaller radii, were closed and, the ratio of the probable water body areas after and before closing the gaps was determined. This ratio was used as one of the input features. After closing the gaps of the binary raster shown in figure 4-13, the resultant raster is shown in figure 4-16. The area was increased by 6.06% which was used as the first input feature of the SVM.
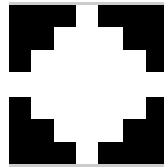
Figure 4-15 Structuring function used for morphological operation
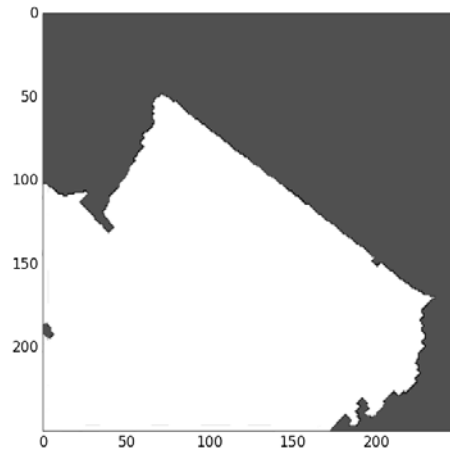
Figure 4-16 Binary raster after closing the gaps of the connected area shown in

figure 4-13

4.6.2 Size of the detected area

The size of the flat area (a probable water body) was chosen to be the second input feature. It was found that elevation profile of land area surrounding a water body changes with the size of the water body. For this reason, the second input feature was used. It was experimentally found that if the natural log of the area of the flat area was selected, the SVM classifier resulted in better classification accuracy. Since water bodies can have a very wide range of areas starting from a fraction of acres to some hundreds of acres, the natural log of the area of a water body is a more elegant input to the SVM classifier. From all the training areas used for training the SVM classifier, 71 flat areas were chosen for training the SVM classifier. Table 4-3 illustrates how the choice of different kernel parameters and input types affect the number of errors in classification (this feature is indicated by *ln(A)* in the table).

4.6.3 Elevation profile of the surrounding area

The surrounding area of a water body must have higher elevation. For this reason, the third input feature was used. A chain of pixels 4 meter away from the probable water body was selected and the number of pixels that have elevation greater than the median elevation of the water surface was counted. The third input feature was chosen to be the ratio of the number of pixels in the surrounding chain of pixels that had elevation greater than the median elevation of the water surface, to the total number of pixels in the chain of surrounding pixels. The value of the third input feature for the flat area in figure 4-13, was found to be 0.9824.

4.6.4 Median elevation difference between the detected area and the surrounding area

The fourth input feature is the natural log of the difference between the median elevation of the surrounding chain of pixels and the median elevation of the probable water body. Taking the natural log of the elevation difference resulted in better classification accuracy than using only the elevation difference as can be seen from the results shown in table 4-3 (this feature is indicated by *In(D)* in the table). For the flat area in figure 4-13, the elevation difference was found to be 40.7479 inches and the natural log of the difference was 3.7074.

4.6.5 Choice of kernel function

The kernel function for SVM generation plays an important role in locating the complex decision boundaries between classes. An inhomogeneous polynomial kernel of the type in equation 4.8 was used for SVM model generation. For best results 'p' in equation 4.8 was experimentally found to be 3.

$$K(x_i, x_j) = (x_i.x_j + 1)^p \qquad\qquad (4.8)$$

Table 4-3 SVM classification error (in percentage) for choice of different kernel

parameters and input types

Inputs	C, A, E, D	C, ln(A), E, D	C, A, E, ln(D)	C, ln(A), E, ln(D)
$p = 1$	73.24	73.24	71.83	71.83
$p = 2$	4.23	4.23	4.23	1.41
$p = 3$	1.41	0	0	0

In table 4-3, '*C', 'A', 'E' and 'D'* represent the first, second, third and fourth input features respectively to the SVM classifier, described in sections 4.6.1, 4.6.2, 4.6.3 and 4.6.4 . '*p'* is the kernel parameter, described in section 4.6.5.

After removing the false detections and adding all the overlapping binary raster tiles, the resultant detected water body is shown in figure 4-17

4.7 Removal of false detections by processing individual probable water bodies

After removing false detections from individual tiles, there might still remain two types of false detections. The first type is tile boundary error. The second type is large flat area false detection error. By processing individual water bodies, these two types of false detections could be removed. The methods to remove those false detections are discussed in the following sections.
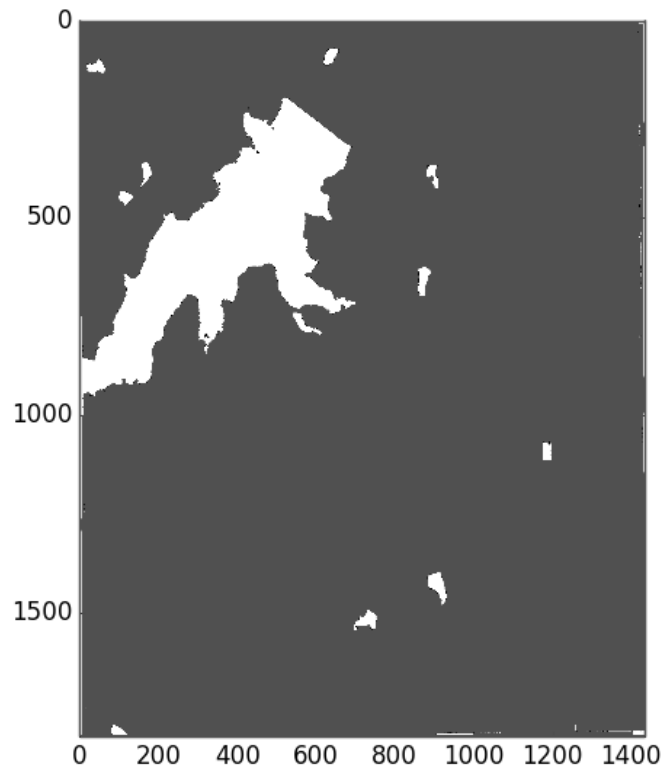
Figure 4-17 Binary raster after removing the false detections and adding all the

overlapping binary raster tiles

4.7.1 Removal of tile boundary false detection error by SVM classifier

Sometimes some flat areas fall near the boundary of a tile and so the boundary of the whole flat area is not available. The SVM classifier developed in this dissertation requires the whole boundary of the water body. Therefore, those flat areas near the tile boundary were falsely detected as water body. An example of false detection due to tile boundary error is shown in light gray shade at the bottom middle part of figure 4-18(a). To remove this type of error, the SVM classification was applied on each detected probable water body. When SVM classification was applied on individual tiles, if the probable water

body fell near the tile boundary, it was not possible to get the chain of pixels in all sides of it. Therefore the SVM method didn't work properly in removing some of those false detections. After processing individual flat areas, the total boundary of the flat area was obtained and the false detections were removed by the same SVM method. The resultant binary raster is shown in figure 4-18(b).

(a) (b) (c)
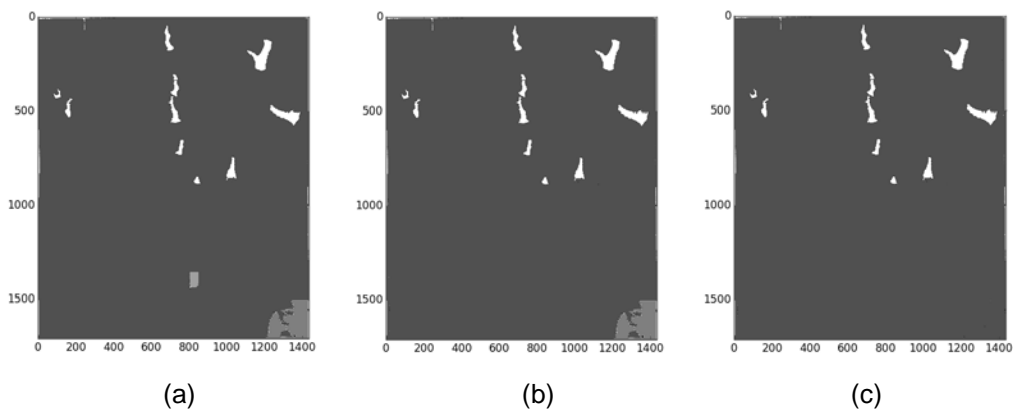
Figure 4-18 (a) Tile boundary false detection error and large flat area false detection error, (b) removal of tile boundary error, (c) removal of large flat area false detection error

4.7.2 Removal of large flat area false detection error by intensity data

The SVM model developed sometimes fails to remove false detection if the size of the flat area or probable water body is greater than 10 acres and the score from the SVM classifier is less than a threshold. In this section, a method is described to remove those false detections using the LiDAR intensity data. LiDAR intensity return from a water body can be of three types:

i) No return due to specular reflection from water surface if the deflection angle is high.

ii)   Very high intensity LiDAR return due to specular reflection if the deflection angle is low.

iii)   Low intensity return since water absorbs very high amount of light energy in near infrared range.

So, LiDAR intensity return from a water surface is significantly different from that of the land area. Large flat area false detection error was removed by using this difference. At first, a rectangular intensity raster was selected, which contained the water body with some extra 50 meters around each side of the water body. Pixels which represented returns from the land and which had intensity less than a threshold (5 times the median intensity of the area) were selected from inside the rectangular area and the mean (μ) and standard deviation (σ) of those pixels were calculated in the intensity raster. Thereafter, all the pixels of the intensity raster, which were from the probable water body were selected and the percentage of those pixels which were within $\mu \pm \sigma$ range of the surrounding area was calculated. If more than a third of the pixels from the probable water body were within the specified range, then the probable water body was identified as a false detection. A large flat land area detected as water body is shown in dark gray shade at the bottom right corner of figure 4-18(a). After removing the false detection, the resultant image is shown in figure 4-18(c).

4.8 Fine-tuning detection using maximum likelihood classification

The approach used for post processing or fine-tuning detection in this dissertation is a modified version of the probabilistic relaxation method described by Eklundh et al. (1980). If the elevation difference between the water surface and its surrounding land area is small, some land pixels could wrongly be classified as water pixels. In those cases, LiDAR intensity data could be used to reclassify those pixels at the

land/water edge. In near infrared range, the reflectivity of water is small compared with vegetation or other topographic features. This property of water was used to fine-tune the detection at the boundary. At first, a rectangular intensity raster was selected, which contained the water body plus 50 meters around each side of the water body and, the mean (μ_l) and standard deviation (σ_l) of the land pixels from inside the rectangular area were calculated. The mean intensity (μ_w) and standard deviation (σ_w) of the pixels identified as water body were also calculated in a similar way. The pixels from which no LiDAR return were recorded and the pixels from which very high intensity LiDAR return were obtained (pixels from which the LiDAR return was 5 times the median intensity of all the LiDAR returns of the area were considered here as high intensity LiDAR returns in this dissertation) were considered outliers and, were not selected for the mean and standard deviation calculations. Two normalized Gaussian curves were plotted as shown in figure 4-19 for LiDAR intensity returns from the detected water body and from its surrounding land area, using the mean and standard deviation values. The maximum likelihood classification method was used only if there were no significant overlap between the normalized Gaussian curves for water and surrounding land area. The overlap between the water and land pixel intensity return distribution was determined by Bhattacharyya distance (BD) given in equation 4.9

$$D_B(l,w) = \tfrac{1}{4} \ln \left(\tfrac{1}{4}\left(\frac{\sigma_l^2}{\sigma_w^2} + \frac{\sigma_w^2}{\sigma_l^2} + 2 \right) \right) + \tfrac{1}{4}\left(\frac{(\mu_l - \mu_w)^2}{(\sigma_l^2 + \sigma_w^2)} \right) \qquad (4\text{-}9)$$

The water pixels at the land water boundary were reclassified only if the BD between the water and land pixel intensity distribution was greater than 0.5. The intersecting point between the normalized Gaussian curves was determined. All the

pixels in the land/water boundary that had intensity greater than the intersecting point intensity but lower than ($\mu_l + 2 \cdot \sigma_l$) and, had elevation greater than the median elevation of the water body were considered as land pixel. Initially, all the pixels that have elevation
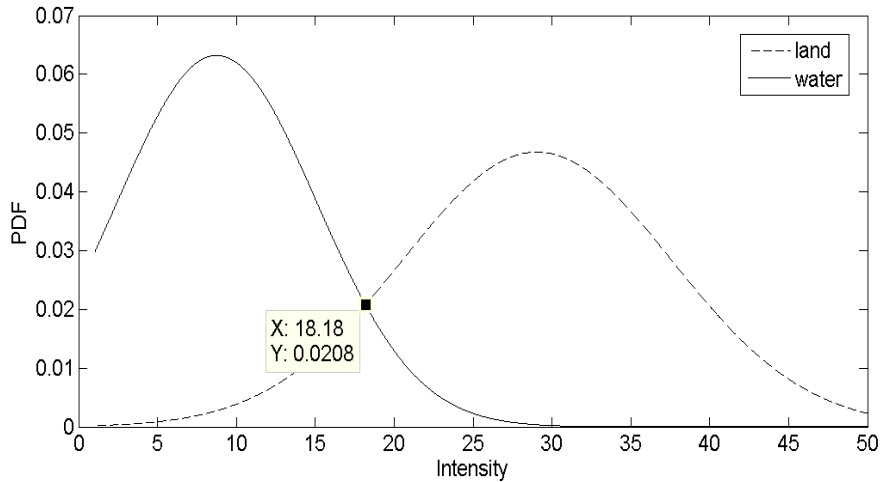
Figure 4-19 Normalized Gaussian curve for intensity return from water surface and from its surrounding land area

less than the upper limit (4 inches) above the median elevation of water surface elevation were considered as returns from water. So the method described here is an attempt to correctly classify the pixels at the land/water boundary that have elevation within the range of 0 to 4 inches above the median surface elevation of the water body. For reclassification, maximum number of iteration used was 11. It was experimentally found that desired result was obtained within 11 iterations.

In figure 4-20, breaklines are shown without using MLC by a red line and manual detection by a black line. A discrepancy is found between the manual detection and the auto detection without MLC.

Bhattacharyya distance for the large water body shown in figure 4-20 was found to be 0.92, which is greater than reclassification threshold of 0.5. After reclassifying the pixels at the boundary, the resultant breakline was found to closely match with the manually generated breakline. The breakline is shown by a green line in figure 4-20.

Figure 4-20 Water body detected with MLC (green line), without MLC (red line) and manually drawn breakline (black line)

4.9 Hydro breakline generation from binary raster

Hydro breaklines are generated from the binary raster of classified pixels. The midpoints of the edges of the binary raster pixels at the detected water/land boundary were automatically connected to generate the breaklines shown in figure 4-21(a). The hydro breaklines were then converted to polygons and, smoothed by Bezier interpolator. The resultant polygon for a water body is shown in figure 4-21(b)

(a)   (b)
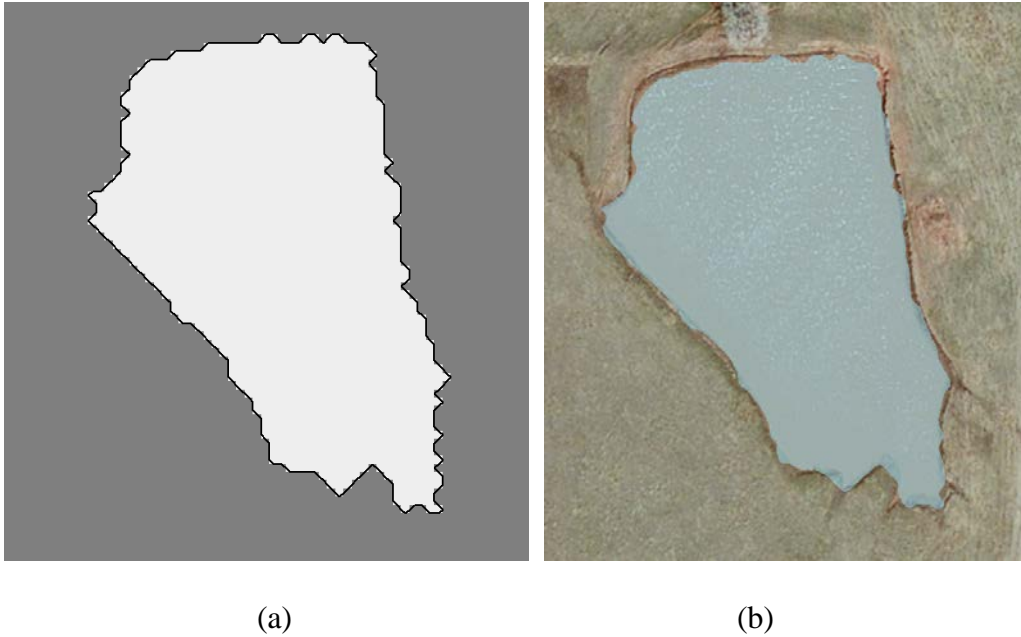
Figure 4-21 Hydro breakline generation: (a) binary raster, (b) smoothed polygons

superimposed on the satellite image

4.10 Results and discussions

To determine the accuracy of classification of land and water, the standard overall accuracy and Cohen's kappa coefficient were used (Foody, 2002). The equations used for the accuracy measurements are

$$\text{Overall accuracy} = \frac{n_{ww} + n_{ll}}{n} \times 100\% \qquad (4.10)$$

$$\text{Kappa coefficient} = \frac{n(n_{ww} + n_{ll}) - (n_{w+}n_{+w} + n_{l+}n_{+l})}{n^2 - (n_{w+}n_{+w} + n_{l+}n_{+l})} \qquad (4.11)$$

where *n* is the total number of LiDAR returns

n_{ww} is the number of returns from water correctly classified as water returns (True positives)

n_{ll} is the number of returns from land correctly classified as land returns (True negatives)

n_{w+} is the total number of returns classified as returns from water by the LASWE algorithm

n_{+w} is the total number of actual returns from water

n_{l+} is the total number of returns classified as returns from land by the LASWE algorithm

n_{+w} is the total number of actual returns from land

Reference data was manually labeled as water or land by a commercial vendor and then re-examined by us. For three different datasets, some areas were chosen for training the algorithm and some areas were chosen for testing the algorithm. The total number of manually classified water and land pixels and correctly classified water and land pixels using the LASWE algorithm is shown in table 4-4. The accuracy of the classification, calculated using equation 4.10 and 4.11, is shown in table 4-5. Only the last returns (in case of multiple returns) and first returns (in case of single return) were classified. For all the test and train areas, overall accuracy was found to be greater than 97.92%. So the LASWE method is comparable with all the other major water surface detection algorithms.

Table 4-4 Number of correctly classified water and land pixels by the LASWE algorithm

Dataset	Testing/ Training	Manual classification		LASWE Classification	
		Total water returns	Total land returns	Correctly classified water returns	Correctly classified land returns
1. Nebraska	Training	1237747	1437832	1222130	1399881
	Testing	944389	9869615	920862	9802166
2. Oklahoma	Training	410545	67990301	392031	67709071
	Testing	224890	64076346	211648	63921455
3. Arkansas	Training	570701	13885271	549263	13674828
	Testing	173022	20336989	1651158	19957973

Table 4-5 Overall accuracy (OA) and κ coefficient for the training and the test areas

Dataset	Size (in sq. km)	Testing/ Training	Overall accuracy (OA)	κ coefficient
1. Nebraska	6.78	Training	98.00	0.96
	22.4	Testing	99.16	0.95
2. Oklahoma	89.61	Training	99.56	0.72
	89.34	Testing	99.74	0.71
3. Arkansas	4.5	Training	98.40	0.82
	6.75	Testing	97.92	0.87

Comparison among different water surface detection algorithm is difficult because each research team applied their algorithm in different geographic location. In table 4-6 the accuracies obtained by different research teams are shown.

Table 4-6 Overall accuracy (OA) range and κ coefficient range for different water surface

detection algorithm

Algorithm/Author	OA range (in percentage)	κ coefficient range
LASWE algorithm	97.92 to 99.74	0.71 to 0.96
Brzank et al. (2008)	94.50 and 99.08	0.82 and 0.98
Smeeckaert et al. (2013)	88.41 to 98.85	0.72 to 0.99
Höfle et al. (2009)	Above 97	Not available

LiDAR return classification for the train area shown in figure 4-3, is shown in figure 4-22. All the true positives (water return detected as water return) are shown by dark blue dots, all the true negatives (land return detected as land return) are shown by cyan dots, all the false positives (water return but detected as land) are shown by green dots and all the false negatives (land but detected as water) are shown by yellow dots. Almost all the wrongly classified pixels are found near the boundary of the water body. LiDAR return classification for another test area is shown in figure 4-23.
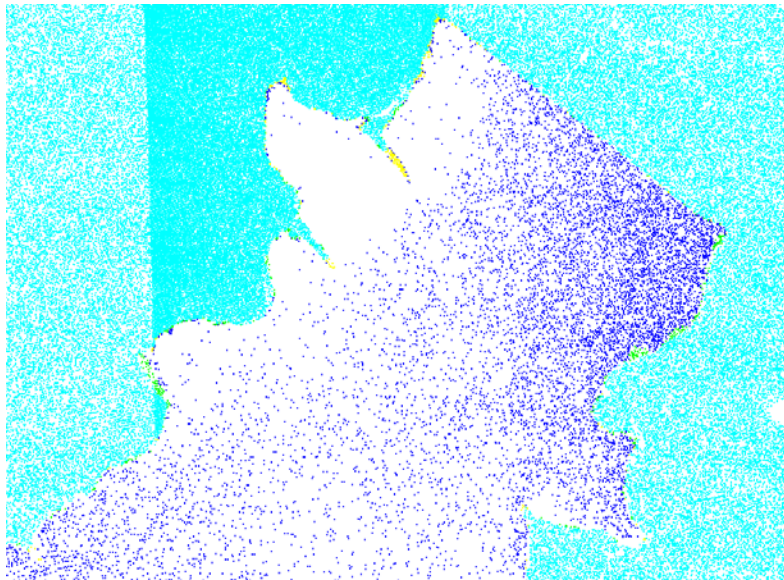
Figure 4-22 LiDAR return classification for the area shown in figure 4-3

51
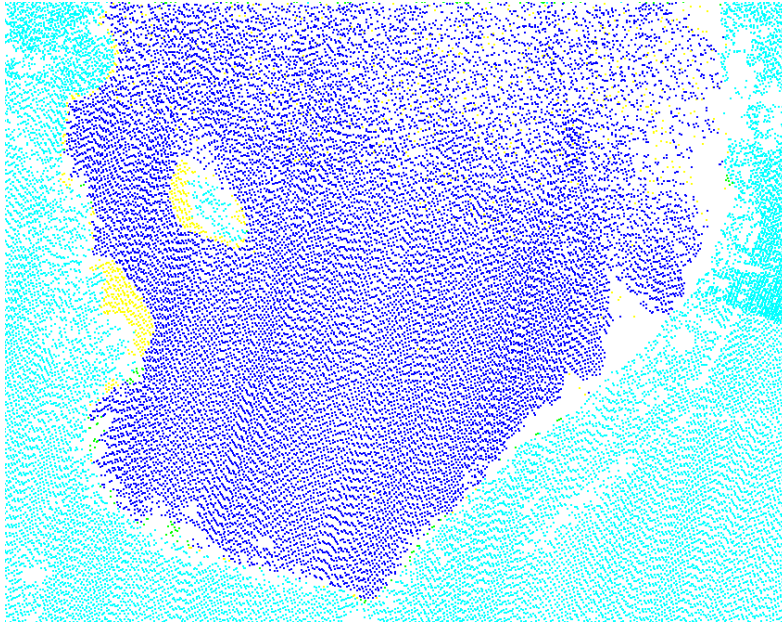
Figure 4-23 LiDAR return classification for a test area in Nebraska

The hydro breaklines generated automatically by the LASWE algorithm were compared with the manually drawn breaklines. In figure 4-24 and 4-25, thin, black lines are the breaklines generated by the LASWE algorithm and the breaklines drawn in manual way are shown by dotted, black lines. From the comparison, it is found that the auto generated hydro breaklines closely matches with the manually generated breaklines.
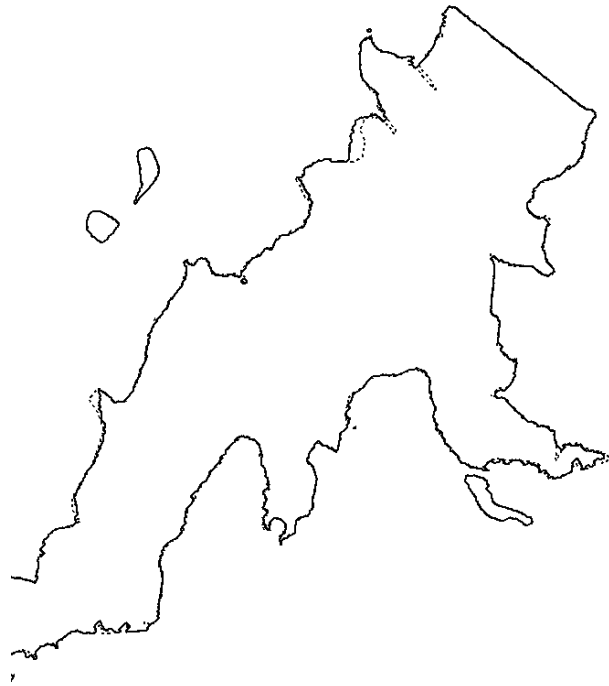
Figure 4-24 LASWE algorithm breakline (solid line) and manual breakline (dashed line)
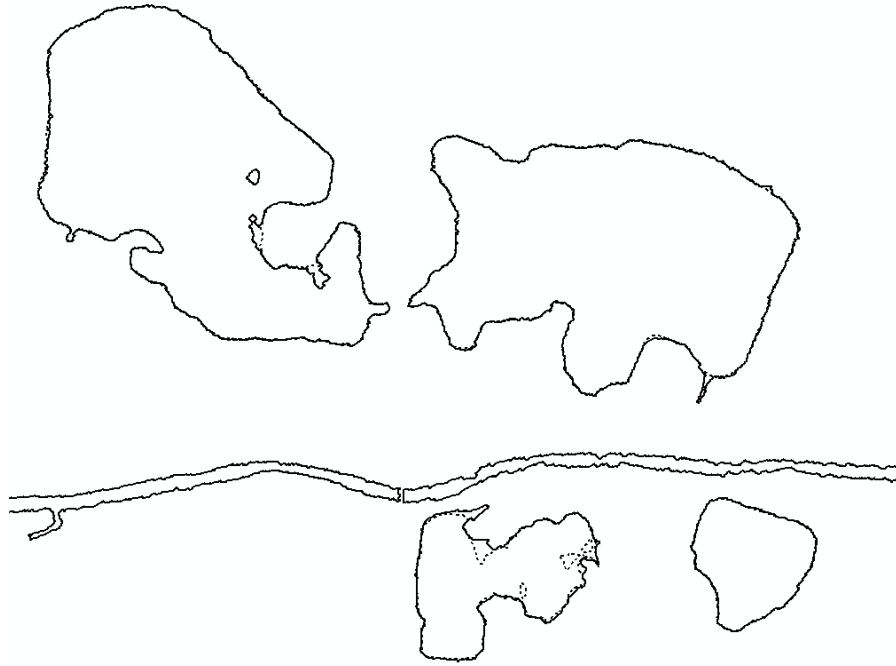
comparison

Figure 4-25 LASWE algorithm breakline (solid line) and manual breakline (dashed line)

comparison

4.11 Conclusions

In this chapter, detailed description of the LASWE algorithm for water body detection is provided. Overall accuracy and kappa coefficient for different test and train area were determined to measure the performance of the algorithm quantitatively. The results were presented in the results and discussion section. The algorithm requires 3 to 9 minutes per sq. km for water surface detection, if LiDAR data density is 0.5 to 4 returns per sq. meter. In the following chapter, a faster and more memory efficient standing water body extraction algorithm is discussed in detail.

Chapter 5

Description of the Multiresolution LASWE Algorithm

5.1 Introduction

The LASWE algorithm requires approximately 3 to 9 minutes per sq. km for water surface detection, if LiDAR data density is 0.5 to 4 returns per sq. meter. The machine used for the detection is a core i7 processor with 16 GB RAM. Some LiDAR projects are very large in size and in those cases, the algorithm requires impractical amount of time. For this reason, the multiresolution LASWE (MLASWE) algorithm was developed. In the MLASWE algorithm, water surface was detected using three different resolutions. The MLASWE algorithm detects all the flat areas that have elevation less than their surrounding areas in coarse resolution. In medium resolution, some of the false detections were removed using both LiDAR elevation and intensity data and the boundary of the water bodies became more precise. In fine resolution, more false detections were removed and the boundaries of water bodies were detected more precisely.

5.2 Description of the coarse-fine integration process for the MLASWE algorithm

The MLASWE algorithm was developed to make the detection of water bodies significantly faster. A coarse-fine integration process was designed for the purpose. The average value of the LiDAR returns from a pixel (n meter by n meter) was used to represent the pixel in the elevation and the intensity raster. In the LASWE algorithm, the median value of the LiDAR returns was used to represent the pixels. Creating median raster is very time consuming. It took about half of the total time required for water surface detection. Moreover, for large size .las files, creation of median raster causes memory exception errors. For all these reasons, the average value was used in the

MLASWE algorithm to represent each pixel, though median value was more preferable for getting a more accurate result. The flow chart of the MLASWE algorithm is shown in figure 5-1.
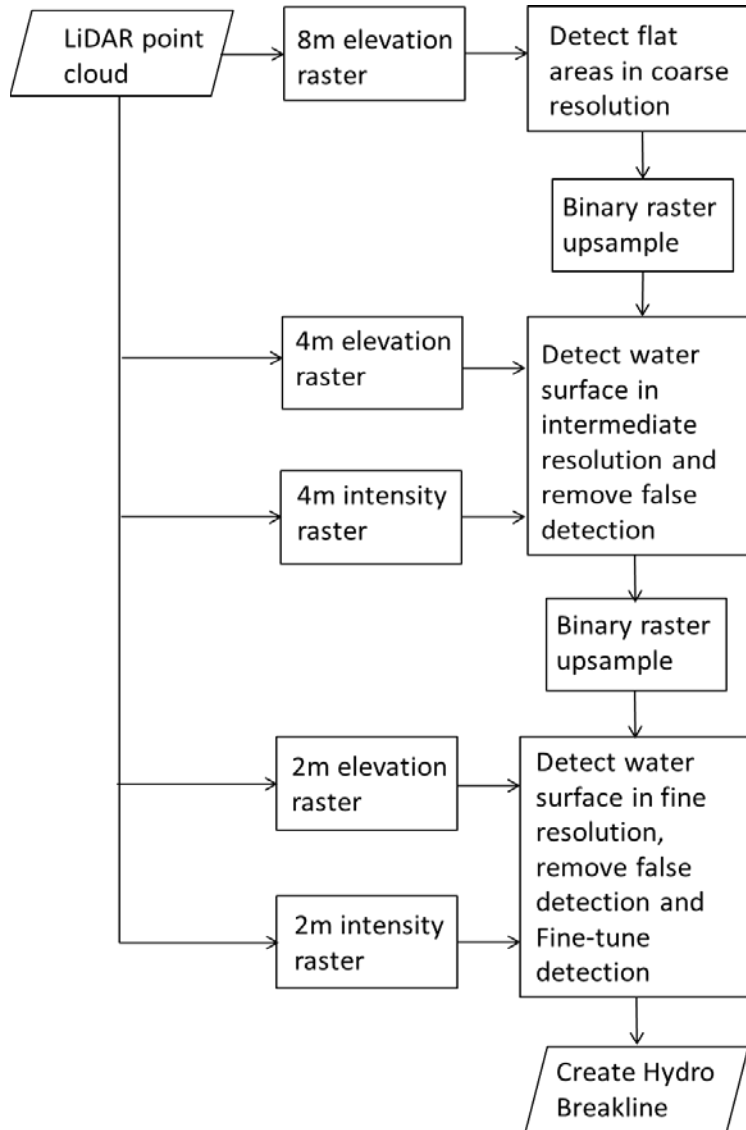
Figure 5-1 Flow chart of the MLASWE algorithm

5.2.1 Flat area detection in a coarse resolution

The first step of the MLASWE algorithm is to detect a water surface in coarse resolution. A coarse 8 meter elevation raster (one sixteenth the resolution of the fine resolution) was created from the LiDAR point cloud. The average value of elevation of the LiDAR returns (first return for single return and last return for multiple returns) from each 8m by 8m cell was used to represent that cell or pixel in the raster. Zero elevation was given to a pixel or cell from which no LiDAR return was recorded. After creating the elevation raster, a histogram was plotted and sharp peaks were detected in overlapping tiles in the same way as in section 4.4 of the previous chapter. For each of those peaks, large connected areas (greater than ¼ acre in size) associated with those peaks were detected as described in section 4.5 of the previous chapter. The MLASWE algorithm was designed to detect all the water surfaces greater than half acre in size. However, in the coarse level all the water surfaces greater than ¼ acre was detected, since in some cases, the entire surface for a water body did not get detected in coarse resolution. In fine resolution detection, only the water bodies greater than ½ acre were retained per our own original specification in the LAWSE.

The median elevations of those flat areas or probable water surfaces along with the median elevations of the surrounding areas were calculated. A chain of pixels 8 meters or 1 pixel away from the flat area was selected to calculate the median elevation of the surrounding area. If the median elevation of the flat area was lower than that of the surrounding area then those flat areas were identified as potential water bodies and analyzed in the medium level resolution. Other flat areas were classified as land areas. At this stage, no SVM classification was applied. It was found that in coarse resolution, if SVM was applied it eliminated some actual water bodies together with the false

detections. The binary raster obtained from coarse resolution elevation raster for an area comprising some test and train area is shown in figure 5-2.

Figure 5-2 Flat areas detected in coarse resolution

5.2.2 Water surface detection in intermediate resolution

In coarse resolution, all the flat areas that have elevation less than that of its surrounding area were detected and a binary raster was obtained as shown in figure 5-2. The binary raster was up-sampled (magnified 400%) by replication (nearest neighbor resampling), for intermediate resolution water surface detection. The flowchart of the intermediate resolution water surface detection is shown in figure 5-3.
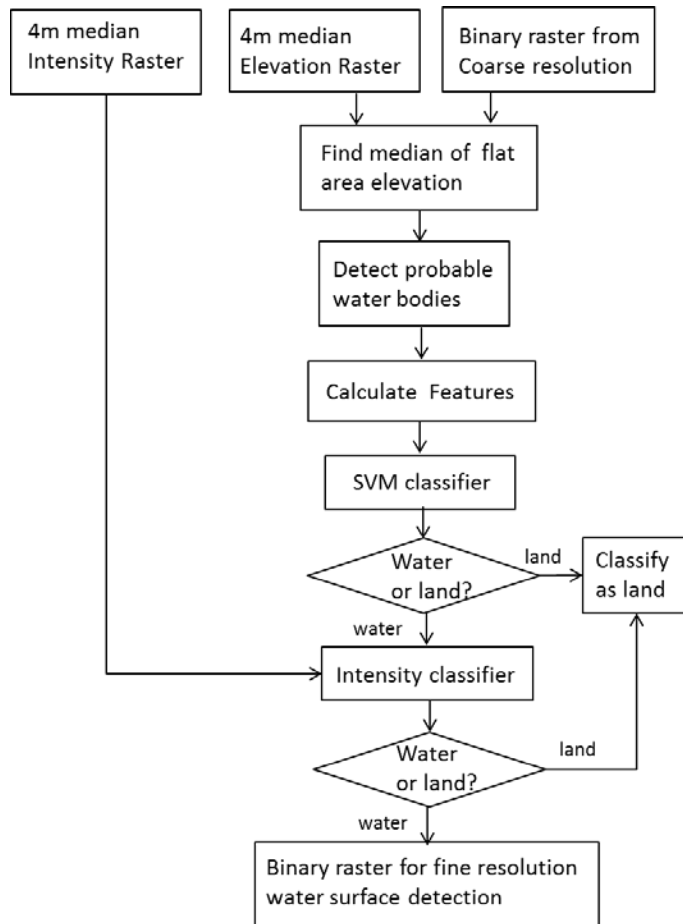
Figure 5-3 Water surface detection in intermediate resolution

5.2.2.1 Intermediate resolution elevation and intensity raster generation

A 4m-elevation and a 4m-intensity raster were generated using the LiDAR point cloud. The average elevation and intensity of the LiDAR returns (first return for single return and last return for multiple returns) from each 4m by 4m cell were used to represent that cell or pixel in the elevation and the intensity raster. Zero elevation and intensity were given to cells or pixels from which no LiDAR return was recorded.

5.2.2.2 Calculation of median elevation of each of the flat areas

The up-sampled binary raster provided the information about all the flat areas in the 4m-elevation raster. Using both the binary raster and elevation raster, it is possible to determine the median elevation of each of the flat areas. Often, inside large flat areas, large connected components were found from which no LiDAR return was recorded. However, inside most of those large connected areas, some scattered pixels were found that had LiDAR returns. Each of the pixels of those large connected areas was given elevation by randomly choosing elevation of the scattered pixels. Thus, the LiDAR returns from water surface were more correctly represented in median water surface elevation calculation.

5.2.2.3 Redetection of flat areas or probable water bodies using median elevation

From the 4m-elevation raster, a rectangular area was selected around each of the flat areas detected in the coarse resolution, with 100 meters extended area in each side. All the pixels that have elevation in the range from [median elevation − 4.8σ_{rms}] to [median elevation + 3σ_{rms}] were detected within the rectangular area. In the LASWE algorithm described in the previous chapter, the lower limit and the upper limit were chosen to be 4.2σ_{rms} and 2.4σ_{rms} respectively. Since the initial detection came from the coarse resolution in the MLASWE algorithm, the median elevation calculated might not be so precise. For this reason, the upper and lower limits were increased by 0.6σ_{rms} in intermediate resolution. However, in fine resolution the upper limit and lower limit were again chosen to be 4.2σ_{rms} and 2.4σ_{rms} respectively.

5.2.2.4 SVM classification and intensity-based classification to remove false detections

After detecting the flat areas or the probable water bodies, the input features for the SVM model were calculated as described in section 4.6 of the previous chapter. For the surrounding area profile calculation, a chain of pixels 8m away from the water surface was selected. After applying the SVM classification, the resultant detection is shown in figure 5-4. In section 4.7.2 of the previous chapter, it was mentioned that some large flat areas could not be removed from the output using the SVM classification. Those false detections were removed by the same method as described in section 4.7.2 of the previous chapter using LiDAR 4m-intensity raster. The resultant binary raster is shown in figure 5-5.

Figure 5-4 Probable water bodies in intermediate resolution after removing the false detections using SVM classification

Figure 5-5 Probable water bodies after classification using LiDAR intensity data

5.2.3 Water surface detection in fine resolution

The binary raster obtained from the intermediate resolution, shown in figure 5-5, was up-sampled (magnified 400%) by replication (nearest neighbor resampling). At this stage, only the SVM classification was carried out. However, the water surface detection was fine-tuned at the boundary using the intensity data. The flowchart of the fine resolution water surface detection is shown in figure 5-6.

A 2m-elevation and intensity raster were created the same way as described in section 5.2.2.1. The median elevation of each of the probable water surface was calculated using the 2m-elevation raster and up-sampled binary raster. Thereafter, each of the water surfaces was redetected using the median elevation value as described in

section 5.2.2.3. However, in fine resolution the upper limit and the lower limit were chosen to be $4.2\sigma_{rms}$ and $2.4\sigma_{rms}$ and the rectangular area was extended by 25 pixels or 50 meter around each side of the water body.
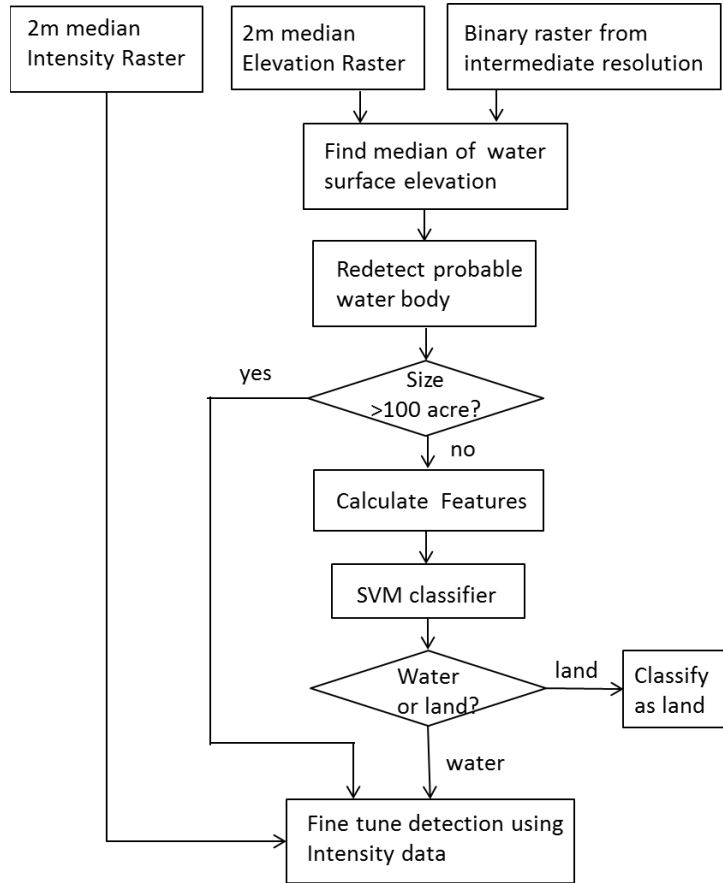
Figure 5-6 Water surface detection in fine resolution

After redetecting the water surface, features were calculated for SVM classifier. Since the SVM classifier does not work well for large flat areas as pointed out on section 4.7.2 of previous chapter and all the probable water surfaces already went through two stages of classification in the intermediate resolution, features were not calculated for the

SVM classifier for water bodies greater than 100 acres in size. Those large flat areas were assumed to be water surfaces without SVM classification to speed up the process of waterbody detection.

After detecting all the water bodies the water surfaces were fine-tuned at the land/water boundary using the LiDAR intensity data in fine resolution the same way as described in section 4.8 of the previous chapter. A water surface from top right corner of figure 5-5 is shown in figure 5-7(b) after fine level detection. The water surface after intermediate resolution detection is shown in figure 5-7(a) for comparison.

<div align="center">(a)   (b)</div>

Figure 5-7 Water surface detected in (a) fine resolution and in (b) intermediate resolution

<div align="center">5.3 Detection of water body from LiDAR data voids</div>

If LiDAR shot dropout rate is very high from the small water bodies, then sometimes in coarse level they did not create a sharp peak in the elevation histogram. To get a sharp peak in the elevation histogram, a large number of LiDAR returns from the water surface are required. The modified elevation histogram discussed in section 4.4.1 of chapter 4 was an attempt to compensate for LiDAR shot dropout. However, some small water bodies greater than half acre in size still remained undetected in coarse resolution even after applying the technique. To detect those water bodies in the 4m-

elevation raster, all the pixels without any LiDAR return were detected. Using connected component analysis, all the connected pixels greater than half acre in size were identified. The binary raster thus obtained was up-sampled for fine level detection. In fine level, all the scattered pixels inside the connected area were detected. The median elevation of those scattered pixels was calculated. All the pixels that have elevation within the range [median elevation − 4.2σ_{rms}] to [median elevation + 2.4σ_{rms}] were added with the pixels that have no LiDAR returns to detect the water pixels. Thus, small water bodies undetected in coarse resolution were detected. One such example is given in figure 5-8. In figure 5-8(a), the connected pixels with no LiDAR returns in the intermediate resolution are shown. In figure 5-8(b), the detected water body in fine resolution is shown.

(a)   (b)
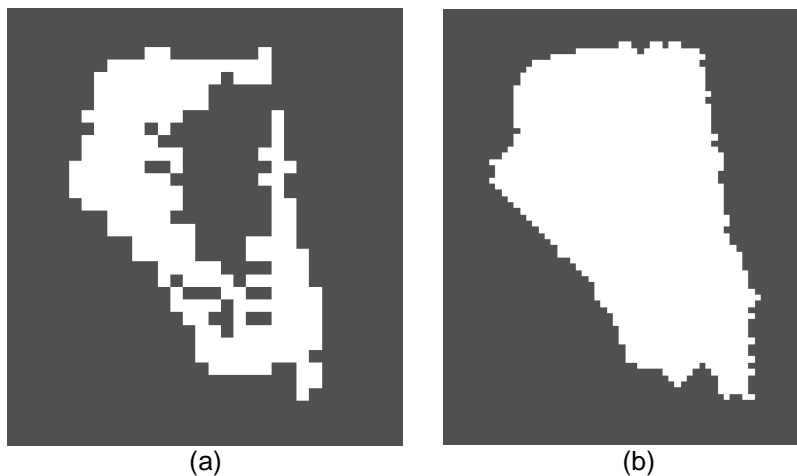
Figure 5-8 Water body detection using LiDAR data voids in (a) intermediate resolution and (b) fine resolution

5.4 Final water body detection in fine resolution

Water body detection by coarse-fine integration discussed in section 5.2 and by LiDAR data voids discussed in section 5.3 were added to get the final detection.

Breaklines were generated from the detection as discussed in section 4.9 of the previous chapter. The hydro breakline polygons superimposed on satellite image are shown by blue colored lines in figure 5-9. Water bodies detected by LiDAR data voids are shown inside white circles in the bottom left corner of the figure.
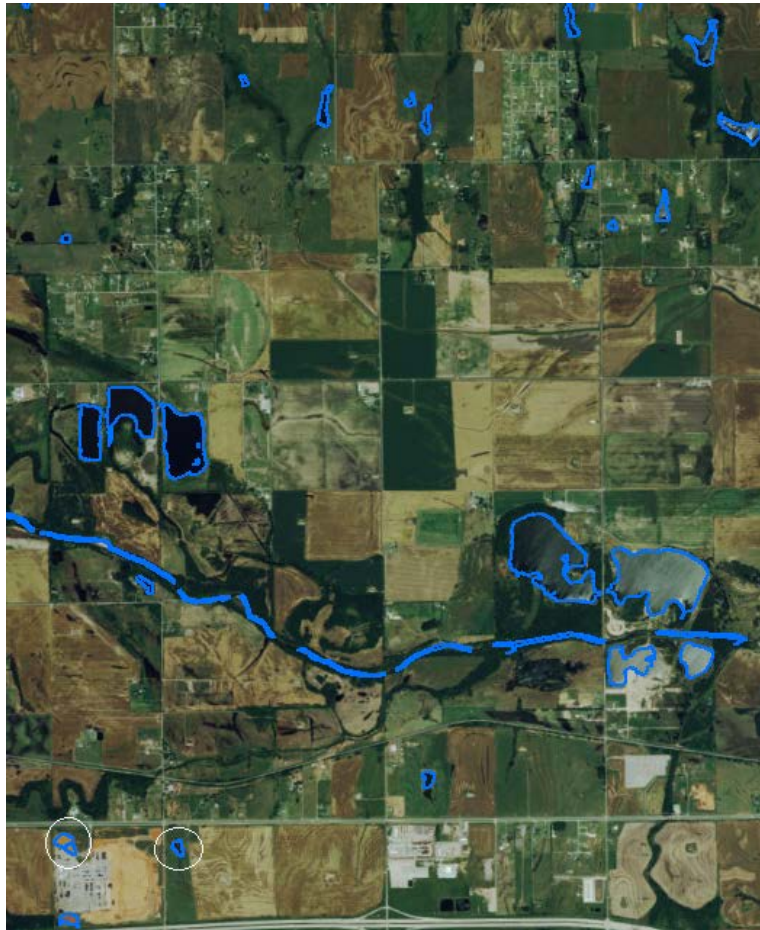
Figure 5-9 Water body detection by coarse-fine integration and by LiDAR void

5.5 Results and discussions

The MLASWE algorithm was applied on the same test and train areas where the LASWE algorithm was applied. Overall accuracy and Cohen's kappa coefficient were

calculated to determine the accuracy of classification. In table 5-1 a comparison is made between the accuracy of the LASWE and the MLASWE algorithm.

From table 5-1, it can be seen that the level of accuracy given by the LASWE and the MLASWE algorithm were almost equal. However, the MLASWE algorithm is almost 15 to 62.5 times faster than the LASWE algorithm. The comparison between the time taken by the LASWE and the MLASWE algorithm is shown table 5-2.

Table 5-1 Comparison of the LASWE and the MLASWE algorithm in terms of accuracy

| Dataset	Testing/ Training	LASWE Classification		MLASWE Classification	
		OA	k	OA	k
1. Nebraska	Training	98.00	0.96	97.66	0.95
	Testing	99.16	0.95	99.11	0.94
2. Oklahoma	Training	99.56	0.72	99.74	0.79
	Testing	99.74	0.71	99.56	0.57
3. Arkansas	Training	98.40	0.82	98.70	0.84
	Testing	97.92	0.87	97.92	0.87

Table 5-2 Comparison of the LASWE and the MLASWE algorithm in terms of speed

Dataset	Testing/ Training	LASWE (in minute per sq. km)	MLASWE (in minute per sq. km)	MLASWE gain
1. Nebraska	Training	2.55	0.25	10.37
	Testing	3.4	0.12	28.33
2. Oklahoma	Training	3.15	0.21	15
	Testing	3.09	0.14	22.56
3. Arkansas	Training	8.84	0.25	35.62
	Testing	8.75	0.14	62.5

Analyzing table 5-2, it can be seen that the LASWE algorithm takes around 3 to 9 minutes for water body detection and breakline generation, whereas the MLASWE algorithm requires approximately 0.12 to 0.25 minutes. The MLASWE algorithm resulted in almost the same classification accuracy as the LASWE, but 15 to 62.5 times faster.

The MLASWE algorithm also does not give any memory exception errors when the .las file is very large in size. Therefore, it can be deduced that the MLASWE algorithm is a faster and memory efficient version of the LASWE algorithm.

Chapter 6

Conclusion and Suggested Future Work

6.1 Contributions

In this doctoral dissertation, a novel approach was taken to detect and delineate water bodies using airborne LiDAR elevation and intensity data. The algorithms developed are called LASWE and MLASWE. Both algorithms provide good classification accuracy for three different sets of train and test areas from different geographical locations. The MLASWE algorithm takes coarse resolution to fine resolution approach, which is much more computationally efficient and faster than the LASWE algorithm.   In our algorithm, an object based segmentation approach was taken to detect water bodies. Finally, since LiDAR data has high vertical accuracy, elevation data weighted than intensity data for water body detection. Intensity data was used when the SVM output is not reliable enough in case of large flat areas and, to classify pixels at the boundary of water bodies when the Bhattacharyya distance between the intensity distribution of LiDAR water surface returns and surrounding area returns were large enough.

The MLASWE algorithm presented in this dissertation is a robust, raster-based method that detects and delineates water surfaces at high speed, in a fully automated mode and with high accuracy.

6.2 Future work

As a future work the following things could be attempted:

1) The standing water body detection algorithm could be extended and modified to detect streams and rivers. Detecting streams and rivers should be challenging, since rivers and streams do not have a constant elevation throughout their path.

69

2) After detecting water bodies using simpler raster based method, LiDAR point cloud data could be used at the boundary of water bodies to get higher classification accuracy.

3) The algorithm developed was applied to three different sets of data to prove its robustness. However, the algorithm could be applied to more areas to make this algorithm a commercial product.

References

Antonarakis, A., Richards, K. S., & Brasington, J. (2008). Object-based land cover classification using airborne LiDAR. *Remote Sensing of Environment*, *112*(6), 2988–2998.

Bartels, M., & Wei, H. (2006). Rule-based improvement of maximum likelihood classified LIDAR data fused with co-registered bands. In *Annual Conference of the Remote Sensing and Photogrammetry Society, CD Proceedings,*. 05–08.

Blaschke, T. (2010). Object based image analysis for remote sensing. *ISPRS Journal of Photogrammetry and Remote Sensing*, *65*(1), 2–16.

Brennan, R., & Webster, T.L. (2006). Object-oriented land cover classification of lidar-derived surfaces. *Canadian Journal of Remote Sensing*, *32*(2), 162–172.

Briese, C., Mandlburgerab, G., Resslb, C., & Brockmannc, H. (2009). Automatic break line determination for the generation of a DTM along the river Main. *Laser scanning, IAPRS, 38(3/W8)*, 236-241

Brzank, A., Heipke, C., Goepfert, J., & Soergel, U. (2008). Aspects of generating precise digital terrain models in the Wadden Sea from lidar–water classification and structure line extraction. *ISPRS Journal of Photogrammetry and Remote Sensing*, *63*(5), 510–528.

Campbell, J. B. (2002). *Introduction to remote sensing*. Taylor & Francis: London..

Charaniya, A. P., Manduchi, R., & Lodha, S. K. (2004). Supervised parametric classification of aerial LiDAR data. CVPRW'04, *Proceedings of the IEEE Conference on Computer Vision and Pattern Recognition Workshop*, *Vol. 3*, (1-8)

Duda, T., Canty, M., & Klaus, D. (1999). Unsupervised land-use classification of multispectral satellite images. A comparison of conventional and fuzzy-logic based clustering algorithms. In *Proceedings of IEEE International Geoscience*

and Remote Sensing Symposium (IGARSS), Hamburg, Germany, 28, 1256–1258.

Eklundh, J.O., Yamamoto, H., & Rosenfeld, A. (1980). A relaxation method for multispectral pixel classification. *Pattern Analysis and Machine Intelligence, IEEE Transactions on, (1)*, 72–75.

Flood, M. (2001). LIDAR activities and research priorities in the commercial sector. *International Archives of Photogrammetry and Remote Sensing, 34(3)*, 3−7.

Foody, G. M. (2002). Status of land cover classification accuracy assessment. *Remote Sensing of Environment*, *80*(1), 185–201.

French, J. (2003). Airborne LiDAR in support of geomorphological and hydraulic modelling. *Earth Surface Processes and Landforms*, *28*(3), 321–335.

Gesch, D. B. (2009). Analysis of Lidar Elevation Data for Improved Identification and Delineation of Lands Vulnerable to Sea-Level Rise. *Journal of Coastal Research*, 49–58. http://doi.org/10.2112/SI53-006.1

Haralick, R. M., & Shapiro, L. G. (1985). Image segmentation techniques. In *1985 Technical Symposium East* (pp. 2–9). International Society for Optics and Photonics.

Heidemann, H. K. (2012). *Lidar base specification.* US Geological Survey.

Höfle, B., Vetter, M., Pfeifer, N., Mandlburger, G., & Stötter, J. (2009). Water surface mapping from airborne laser scanning using signal intensity and elevation data. *Earth Surface Processes and Landforms*, *34(12),* 1635–1649.

Höfle, B., & Pfeifer, N. (2007). Correction of laser scanning intensity data: Data and model-driven approaches. *ISPRS Journal of Photogrammetry and Remote Sensing*, *62(6)*, 415–433.

Hollaus, M., Wagner, W., & Kraus, K. (2005). Airborne laser scanning and usefulness for hydrological models. *Advances in Geosciences*, *5(5)*, 57–63.

Huang, C., Davis, L. S., & Townshend, J. R. G. (2002). An assessment of support vector machines for land cover classification. *International Journal of Remote Sensing*, *23(4)*, 725–749.

Jelalian, A. V. (1992). *Laser radar systems. Artech House. Bosten und London*, p. 292

Jenkins, R. B., & Frazier, P. S. (2010). High-resolution remote sensing of upland swamp boundaries and vegetation for baseline mapping and monitoring. *Wetlands*, *30*(3), 531–540.

Jensen, J. R. (2009). *Remote sensing of the environment: An earth resource perspective 2/e*. Pearson Education India.

Jones, A. F., Brewer, P. A., Johnstone, E., & Macklin, M. G. (2007). High-resolution interpretative geomorphological mapping of river valley environments using airborne LiDAR data. *Earth Surface Processes and Landforms*, *32(10)*, 1574–1592.

Lane, C. R., & D'Amico, E. (2010). Calculating the ecosystem service of water storage in isolated wetlands using LiDAR in North Central Florida, USA. *Wetlands*, *30(5)*, 967–977.

Lang, M. W., & McCarty, G. W. (2009). Lidar intensity for improved detection of inundation below the forest canopy. *Wetlands*, *29(4)*, 1166–1178.

Liu, H., Wang, L., Sherman, D. J., Wu, Q., Su, H., & others. (2011). Algorithmic foundation and software tools for extracting shoreline features from remote sensing imagery and LiDAR data. *Journal of Geographic Information System*, *3(02)*, 99.

Liu, J.K., Li, R., Deshpande, S., Niu, X., & Shih, T.Y. (2009). Estimation of blufflines using topographic Lidar data and orthoimages. *Journal of Photogrammetric Engineering and Remote Sensing*, *75(1)*, 69–79.

Otsu, N. (1975). A threshold selection method from gray-level histograms. *Automatica*, *11*(285-296), 23–27.

Petrie, G., & Toth, C. K. (2008). *Introduction to laser ranging, profiling, and scanning. Topographic Laser Ranging and Scanning: Principles and Processing.* CRC Press Taylor Francis: London, UK. 1-28

Rutzinger, M., Hoefle, B., & Kringer, K. (2012). Accuracy of automatically extracted geomorphological breaklines from airborne LiDAR curvature images. *Geografiska Annaler: Series A, Physical Geography*, *94(1)*, 33–42.

Sahoo, P. K., Soltani, S., & Wong, A. K. (1988). A survey of thresholding techniques. *Computer Vision, Graphics, and Image Processing*, *41(2)*, 233–260.

Schmid, K., Waters, K., Dingerson, L., Hadley, B., Mataosky, R., Carter, J., & Dare, J. (2008). Lidar 101: An introduction to lidar technology, data, and applications. *NOAA Coastal Services Center*, 76.

Smeeckaert, J., Mallet, C., David, N., Chehata, N., & Ferraz, A. (2013). Large-scale classification of water areas using airborne topographic lidar data. *Remote Sensing of Environment*, *138*, 134–148.

Southwell, R. V. (1940). Relaxation Methods in Engineering Science, A Treatise on Approximate Computation, Oxford Univ. Press, London

Sun, W., Heidt, V., Gong, P., & Xu, G. (2003). Information fusion for rural land-use classification with high-resolution satellite imagery. *Geoscience and Remote Sensing, IEEE Transactions on*, *41(4)*, 883–890.

Toscano, G., Gopalam, U., & Devarajan, V. (2013). A novel method for automation of 3D hydro break line generation from LiDAR data using MATLAB. *ISPRS-International Archives of the Photogrammetry, Remote Sensing and Spatial Information Sciences*, *1*(2), 99–104.

Toscano, G., Gopalam, U., & Devarajan, V., (2014). Auto Hydro Break Line Generation Using LiDAR Elevation and Intensity Data. *Proceedings, ASPRS Conference, Louisville, Kentucky.*

Toscano, G., Acharjee, P., McCormick, C. & Devarajan, V., (2015). Water Surface Elevation Calculation Using LiDAR Data. *Proceedings, ASPRS Conference, Tampa, Florida.*

Wang, L., Sousa, W., & Gong, P. (2004). Integration of object-based and pixel-based classification for mapping mangroves with IKONOS imagery. *International Journal of Remote Sensing*, *25(24),* 5655–5668.

Wolfe, W., Zissis, G.J., 1989. *The infrared handbook. In: The Infrared Information Analysis Center*. Environmental Research Institute of Michigan, Detroit, p. 1700.

Biographical Information

George John Toscano received a B.Sc. in Electrical and Electronic engineering, in 2005 from Bangladesh University of Engineering and Technology (BUET), Dhaka, Bangladesh. He received an M.SC. in Electronic and Communication engineering from the same university in 2008. He earned his PhD in Electrical Engineering at the University of Texas at Arlington, Arlington, Texas in 2015. His research interests are in image processing, computer vision, machine learning and remote sensing with LiDAR.